A PRECLINICAL ARBITRARY WAVEFORM MAGNETIC PARTICLE IMAGING SCANNER FOR MULTI-FREQUENCY IMAGING

A THESIS SUBMITTED TO

THE GRADUATE SCHOOL OF ENGINEERING AND SCIENCE

OF BILKENT UNIVERSITY

IN PARTIAL FULFILLMENT OF THE REQUIREMENTS FOR

THE DEGREE OF

MASTER OF SCIENCE

IN

ELECTRICAL AND ELECTRONICS ENGINEERING

By

Beril Alyüz Yilmaz

August 2023

A PRECLINICAL ARBITRARY WAVEFORM MAGNETIC PARTICLE IMAGING SCANNER FOR MULTI-FREQUENCY IMAGING
By Beril Alyüz Yilmaz
August 2023

We certify that we have read this thesis and that in our opinion it is fully adequate, in scope and in quality, as a thesis for the degree of Master of Science.

Emine Ülkü Sarıtaş Çukur(Advisor)

Ergin Atalar

Yeşim Serinağaoğlu Doğrusöz

Approved for the Graduate School of Engineering and Science:

Orhan Arıkan
Director of the Graduate School

ABSTRACT

A PRECLINICAL ARBITRARY WAVEFORM MAGNETIC PARTICLE IMAGING SCANNER FOR MULTI-FREQUENCY IMAGING

Beril Alyüz Yilmaz
M.S. in Electrical and Electronics Engineering
Advisor: Emine Ülkü Sarıtaş Çukur
August 2023

Magnetic Particle Imaging (MPI) is a tracer based tomographic imaging modality that images the spatial distribution of the magnetic nanoparticles (MNPs) using their nonlinear magnetization response. MPI is a rapidly growing and safe imaging modality with high temporal and spatial resolution, together with high sensitivity. In MPI, different types of MNPs and the properties of their local environment such as viscosity and temperature can be identified via the relaxation behavior of the MNPs. The optimal drive field (DF) frequency depends on the application of interest. In addition, the sensitivity of quantitative mapping can benefit from imaging at multiple DF frequencies. However conventional MPI systems utilize an impedance matching circuitry tuned to a specific DF frequency to mitigate the reactive power, which in turn restricts the operation of the MPI systems to that frequency. In this thesis, a preclinical arbitrary waveform (AW) MPI scanner is proposed to enable flexible functionality in a wide range of operating frequencies. The AW MPI scanner features three specialized components: (1) an AW drive coil with a reduced inductance achieved by utilizing Rutherford cable windings to enable wideband imaging in a preclinical-size MPI scanner, (2) a gradiometric receive coil designed to have zero mutual inductance with the AW drive coil to alleviate the effect of the direct feedthrough signal while sensitively receiving the MNP signal, and (3) additional capacitor banks to block DC current while avoiding distortions in the DF waveform. This thesis also proposes a technique for multi-frequency imaging in a single scan using the developed AW MPI scanner. Experimental imaging results demonstrate that MPI images and relaxation maps can be successfully achieved at multiple DF frequencies using the developed AW MPI scanner and the proposed multi-frequency imaging technique.

Keywords: Magnetic particle imaging, arbitrary waveform, multi-frequency imaging, relaxation mapping, quantitative mapping.

ÖZET

ÇOK FREKANSLI GÖRÜNTÜLEME İÇİN PREKLİNİK RASTGELE DALGA FORMU MANYETİK PARÇACIK GÖRÜNTÜLEME TARAYICISI

Beril Alyüz Yilmaz
Elektrik ve Elektronik Mühendisliği, Yüksek Lisans
Tez Danışmanı: Emine Ülkü Sarıtaş Çukur
Ağustos 2023

Manyetik Parçacık Görüntüleme (MPG) manyetik nanoparçacıkların (MNP) uzaysal dağılımını, onların doğrusal olmayan manyetizasyon tepkisini kullanarak görüntüleyen iz sürücü tabanlı bir tomografik görüntüleme yöntemidir. MPG yüksek zamansal ve uzaysal çözünürlüğe ve yüksek duyarlılığa sahip, hızla gelişen ve güvenli bir görüntüleme yöntemidir. MPG'de farklı tip MNP'ler ve onların viskozite ve sıcaklık gibi lokal ortam özellikleri, MNP'lerin relaksasyasyonu aracılığıyla belirlenebilir. Optimum eksitasyon alanı (EA) frekansı hedeflenen uygulamaya bağlıdır. Ayrıca, niceliksel haritalamanın duyarlılığı birden fazla EA frekansında görüntülemeden faydalanabilir. Ancak, konvensiyonel MPG sistemleri reaktif gücü azaltmak için belirli bir EA frekansına ayarlanmış empedans eşleştirme devresi kullandığı için tek frekansa kısıtlıdır. Bu tezde, geniş bir çalışma frekansı aralığında esnek işlevsellik sağlamak için bir preklinik rastgele dalga formu (RDF) MPG tarayıcısı önerilmektedir. RDF MPG tarayıcısı üç özel bileşene sahiptir: (1) Preklinik boyutlu bir MPG tarayıcıda geniş bant görüntülemeyi mümkün kılmak için Rutherford kablo sarımları kullanılarak azaltılmış endüktansa sahip bir RDF sürücü bobini, (2) hassas bir şekilde MNP sinyalini alırken doğrudan besleme sinyalinin etkilerini hafifletmek için RDF sürücü bobini ile sıfır karşılıklı endüktansa sahip olacak şekilde tasarlanmış bir gradyometrik sinyal alıcı bobin, (3) DC akımını bloke ederken EA dalga formunda bozukmalardan kaçınmak için ek kapasitans bankaları. Ayrıca, bu tez geliştirilen RDF MPG tarayıcısını kullanarak tek taramada çok frekanslı görüntüleme için bir teknik önermektedir. Deneysel görüntüleme sonuçları, geliştirilen RDF MPG tarayıcısı ve önerilen çok frekanslı görüntüleme tekniği ile MPG görüntülerinin ve relaksasyasyon haritalarının çoklu EA frekanslarında başarılı bir şekilde elde edilebileceğini göstermektedir.

Anahtar sözcükler: Manyetik parçacık görüntüleme, rastgele dalga formu, çok frekanslı görüntüleme, relaksasyon haritalama, niceliksel haritalama.

Acknowledgement

First of all, I would like to thank my advisor, Assoc. Prof. Emine Ülkü Sarıtaş, for her invaluable support and supervision. It has been an honor and a privilege to work with her. She has been a source of inspiration and a role model for me ever since I started working with her during my Bachelor's degree. I am forever grateful for her attentiveness, understanding, and skillful guidance during my Bachelor's and Master's degrees.

I would also like to thank Prof. Ergin Atalar and Assoc. Prof. Yeşim Serinağaoğlu Doğrusöz for being on my master's thesis committee. I greatly valued and deeply appreciated their feedback on my work.

I would like to thank the Scientific and Technological Research Council of Turkey (TUBITAK Grant No: 120E208, 122E162, 217S069, 120E346) for supporting the work in this thesis.

I would like to thank my colleagues in our research group: Aslı Alpman, Abdallah Zaid Alkinali, Atakan Topçu, Ege Kor, Sefa Karaca, Bahadır Alp Barlas, Elif Aygün, Ecrin Yağız, Ali Alper Özaslan, Musa Tunç Arslan, and Mustafa Ütkür. I would like to give my special thanks to my closest friend Aslı, who has been a constant source of strength and encouragement throughout my journey. I wish to express my sincere appreciation to Abdallah, Sefa, Atakan, and Ege for their friendship and constant positivity. I extend my heartfelt appreciation to Bahadır, Elif, Ecrin, and Mustafa for their enduring friendship and the unwavering support they have continued to provide, even after their graduation. I would like to thank Ali Alper, Musa Tunç, and Mustafa for helping me with the experiment setup and procedures. Additionally, I would like to express my gratitude to Musa Tunç and Mustafa for assisting me during my introduction to the laboratory.

I would like to express my deepest gratitude to my parents, Afitap and Hasan Yaşar Alyüz, for their endless encouragement and belief in my academic pursuits. I am sincerely thankful for the opportunities they provided me to pursue higher education.

Finally, I want to extend my deepest appreciation to my husband, Kerem Yilmaz, for his enduring love and encouragement. I am deeply grateful for his presence in my life and for being my rock when I needed it the most. His constant faith in my abilities has been a constant source of strength for me. This thesis is a testament to the enduring support of my parents and my husband, and I dedicate it to them with all my heart.

Contents

List of Figures

List of Tables

Chapter 1

Introduction

The ability to visually represent the inner human body has significantly facilitated the diagnosis and treatment processes for several diseases. Magnetic resonance imaging (MRI), x-ray imaging, computed tomography (CT), ultrasound, single photon emission computed tomography (SPECT), and positron emission tomography (PET) are examples of prevalent medical imaging modalities. MRI, CT, SPECT, and PET are classified as tomographic imaging modalities, producing slice-by-slice images of a selected part of the human body. MRI and CT directly image the proton density and X-ray attenuation, respectively, while contrast materials can also be used to enhance image contrast [1]. In contrast, nuclear imaging methods such as PET and SPECT image the spatial distribution of a radioactive tracer administered into the human body prior to imaging. These tracer based imaging modalities are broadly used for cancer detection and functional imaging, since tracers interact with the metabolism to reveal disease indications. However, they cannot identify details about the background human anatomy since the detected signals only come from the applied tracers.

Magnetic Particle Imaging (MPI) is a novel tracer based tomographic imaging modality that images the spatial distribution of magnetic nanoparticles (MNPs) by exploiting their nonlinear magnetization response [2]. The most commonly used MNPs for MPI are superparamagnetic iron oxide (SPIO) nanoparticles since they are safe to administer to human subjects (even for patients with chronic kidney disease) and have already been used as clinically approved contrast agents in MRI [3].

MPI directly receives signal from the MNPs with zero signal from the background tissue. Therefore, it offers superior sensitivity for detecting MNPs when compared to MRI. In MRI, MNPs have negative contrast due to T_2^* dephasing, which makes their precise localization difficult [3]. MPI can provide high temporal and spatial resolution, potentially allowing applications with fast, dynamic imaging requirements [4]. Unlike x-ray and CT, MPI does not utilize ionizing radiation, making it a safer alternative. Additionally, unlike PET and SPECT, MPI does not use radioactive tracers that cause ionizing radiation [1]. First introduced in 2005 and rapidly developing since then, MPI has already been demonstrated for several applications such as angiography [5, 6], stem-cell tracking [7, 8, 9], cardiovascular interventions [10], cancer imaging [11], drug delivery [12, 13], and localized hyperthermia [14].

In MPI, three different magnetic fields are employed to image the spatial distribution of MNPs. A static selection field (SF) with strong spatial gradients enables the localization of the MNP signal. SF creates a zero-field area at the center of the scanner setup, referred to as the field-free region (FFR). The FFR is rapidly moved across the field-of-view (FOV) by using a sinusoidal drive field (DF) to generate time-varying magnetization. A receive coil records the signal induced by the change in MNP magnetization. Because of human safety and hardware limitations, DF alone is not adequate to cover the entire FOV [15, 16]. Hence, FOV is separated into smaller regions called partial field-of-views (pFOVs). To achive this, a high-amplitude and low-frequency focus field (FF) shifts the FFP to areas that cannot be reached by the DF alone [17, 18, 19].

System Function Reconstruction (SFR) and X-space reconstruction are the two widely used image reconstruction methods in MPI. For SFR, the FOV is divided into voxels, and a system matrix (SM) is obtained by recording the induced particle signal from a point source MNP at each voxel location [20]. SM explains the linear relationship between the MNP distribution and the measurement signal. The MPI image is obtained by solving a linear system of equations [21]. However, achieveing a high resolution reconstruction demands a long calibration scan of a point source MNP. Moreover, the SM is not generalizable and needs to be measured separately for different MNPs and/or different scanning trajectories. In contrast, X-space reconstruction achieves the reconstruction of the spatial distribution of the MNPs in real-time by gridding the induced signal to the instantaneous position of the FFR. X-space reconstruction does not require calibration scans, but the point spread function of the system causes a blurring in the reconstructed MPI images [22, 23].

In MPI, the relaxation behavior of MNPs causes a delay in the alignment between their magnetic moments and the applied DF, which causes a loss in signal-to-noise (SNR) and blurring in the MPI image due to a peak shift and an amplitude loss in the MPI signal [24]. MNPs have distinct MPI signals controlled by their physical properties such as their magnetic material and core size [3]. Furthermore, MNPs can exhibit different relaxation behaviors depending on their local environmental conditions such as temperature and viscosity [24]. Color MPI is a quantitative mapping application that aims to differentiate different MNP types and their environment by exploiting these variations in the MNP signal. Color MPI expands the application spectrum of MPI, including MNP-labeled catheter tracking for vascular interventions [25, 26], catheter steering during endoscopic procedures [27], and viscosity [28, 29, 30, 31, 32, 33] and temperature mapping [34, 35, 36, 33].

Reducing the reactive power on the power amplifier is crucial for achieving DF amplitudes large enough to excite the MNPs. Conventional MPI scanners require impedance matching to manage the reactive power, which restricts their operation to a single frequency [37]. Limiting the scanner operation to a particular frequency is inconvenient for quantitative mapping applications where the optimal DF parameters depend on the application of interest [31, 33]. Additionally, since MNP signal changes with DF parameters, having a flexible system can facilitate and accelerate the optimization process of DF parameters. Reducing the inductance of the DF coil decreases the reactive power while providing performance in a wide bandwidth, enabling arbitrary waveform (AW) characteristics. Previously, other studies miniaturized the DF coil to reduce its inductance and allow AW characteristics for magnetic particle spectrometer and relaxometer setups [38, 39, 40]. Furthermore, magnets were added to an AW relaxometer in order to achieve small-scale field free line MPI scanner for enabling pulsed excitation in MPI [41]. In this thesis, the design of a DF coil that achieves AW characteristics in a typical-sized preclinical MPI scanner is proposed. The design utilizes Rutherford cable windings and achieves a 144-fold reduction in inductance compared to a standard DF coil [37]. Additionally, a gradiometric receive coil is designed to effectively mitigate the direct feedthrough signal, achieving approximately 65 dB decoupling between drive and receive coils [42]. In Chapter 3, the designs of the DF coil and the receive coil are presented with simulation results and demonstrated via imaging experiments on an FFL MPI scanner at two distinct sinusoidal DF waveforms at 2.5 kHz and 5 kHz.

As previously mentioned, MNP signal depends on their physical properties and environmental conditions, as well as the DF parameters. Therefore, the optimal DF parameters differ depending on the quantitative mapping application [33, 43]. In addition, measurements at different DF settings may be required to accurately distinguish distinct MNP types or their local environments [33]. In Chapter 4, this thesis proposes a technique for single-pass imaging and relaxation mapping at multiple frequencies using the developed AW MPI scanner. This technique forms a DF waveform by continuously stacking a fixed number of periods of selected DF settings at multiple frequencies one after another. The low inductive reactance of the designed AW DF coil permits flexible functionality in a wide bandwidth. The results of 1D and 2D imaging experiments demonstrate the proposed AW MPI scanner and the multi-frequency imaging technique can successfully produce images and relaxation maps at multiple frequencies. The techniques proposed in this thesis have the porential to increase the accuracy and reduce the scan time for quantative mapping application of MPI.

Chapter 2

Background on Magnetic Particle Imaging (MPI)

2.1 Imaging Principles

Magnetic Particle Imaging (MPI) spatially resolves the local concentration of magnetic nanoparticles (MNPs) by utilizing their nonlinear magnetization behavior. As depicted in Figure 2.1(a), the particle magnetization increases rapidly for a range of applied field strengths, then stabilizes even when the external magnetic field continues to grow. The Langevin function can be used to model overall particle magnetization behavior as follows [1, 2, 22]:

$$M(H) = c\ m\ \mathcal{L}(kH) = c\ m\left(coth(kH) - \frac{1}{kH}\right) \tag{2.1}$$

where

$$k = \frac{\mu_0 m}{k_B T}. \tag{2.2}$$

Here, M is the particle magnetization, c is the particle concentration in units of particles/m^3, m is a single MNP's magnetic moment, H is the applied magnetic field, μ_0 is the vacuum permeability, k_B is the Boltzmann constant, and T is the temperature in Kelvin. In addition, $m = M_{sat}\pi d^3/6$ for a single domain spherical MNP with core diameter d, and $M_{sat} = 0.6\ T/\mu_0$ for magnetite MNPs [22].

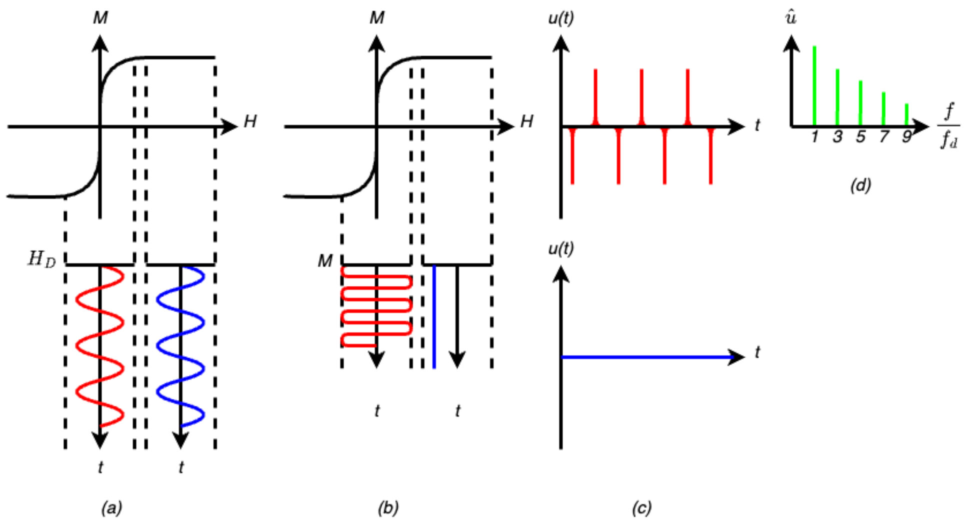

Figure 2.1: (a) MNP magnetization M vs. the applied magnetic field H. H_D denonotes a sinusoidal drive field (DF) that is applied to induce magnetization response. Red curve denotes the case of MNPs that are in a field free region (FFR) and blue curve denotes the case of MNPs with saturated magnetization. (b) MNP magnetization vs. time t. Only the MNPs in the FFR generate a magnetization response (red curve). Saturated MNPs do not respond to the applied DF (blue curve). (c) MNP signal acquired via induction vs. time t. The MNPs in FFR generate a received signal (red curve). There is no induced signal from the saturated MNPs (blue curve). (d) Frequency spectrum of the received signal. The signal is at the harmonics of the applied fundamental frequency f_d.

Figure 2.1 summarizes the imaging procedure. A sinusoidal DF (referenced as H_D in Figure 2.1(a)) is applied to MNPs. Due to the magnetization response of the MNPs, only the MNPs in a field free region (FFR) are excited by the DF as shown in red curves in Figure 2.1. In contrast, the MNPs that have saturated magnetization cannot respond to the applied DF, as depicted in blue curves in Figure 2.1. Therefore, only the response of the MNPs in FFR is recorded and the MNPs in saturated regions have zero response, as illustrated in Figure 2.1(c). Figure 2.1(d) depicts the Fourier transform of the recorded MNP response, which is at the harmonics of the fundamental frequency (i.e., the frequency of the applied sinusoidal DF).

2.2 Imaging Scanner

A conventional MPI scanner uses three main magnetic fields to image the spatial distribution of the MNPs: (1) a static selection field (SF) to select a region in space as the FFR and measure the amount of magnetic material present at that region, (2) a sinusoidal drive field (DF) with sufficient amplitude to reveal whether a magnetic material is present or not, and (3) a slowly varying focus field (FF) to extend the field-of-view and move the FFR to locations that DF cannot be reached with the DF alone [1]. These fields can be generated by dedicated or shared coils [44]. The MNP response to time-varying magnetic field is then received via induction by a receive coil.

2.2.1 Selection Field

Figure 2.1 summarizes the nonlinear magnetization of MNPs and its utility for spatial encoding in MPI. SF features a static magnetic field gradient with a FFR, usually achieved by situating two permanent magnets with the same poles facing each other [45, 17] or two electromagnets in Maxwell configuration [46] Depending on the configuration of the magnets, FFR can be a field-free point (FFP) as depicted in Figure 2.2, or a field-free line (FFL) as depicted in Figure 2.3. The field strength in the SF rapidly increases in regions away from the FFR, forcing the MNPs outside FFR into saturation. Therefore, only the MNPs in the close vicinity of FFR have magnetizations in the dynamic range and can react to the sinusoidal DF as shown in Figure 2.1(b), enabling a direct link between the received MNP signal and FFR location [1].

The SF has different magnetic field gradients along different directions. These gradients satisfy $G_x + G_y + G_z = 0$, where G_i is the gradient along the direction i. While choosing the gradient of the SF, it is important to make sure that the magnetic field from the DF is sufficiently larger than the DF amplitude within the imaging volume.

2.2.2 Drive Field

The sinusoidal DF superimposed on top of the SF is responsible for moving the FFR back and forth along its field vector direction during the measurement. The DF enables acquiring signals from MNPs at several voxels along the FFP trajectory rather than at a single voxel [1, 2]. For a sinusoidal DF along x with amplitude H_{peak} and frequency f_d, i.e., $H_d(t) = H_{peak}cos(2\pi f_d t)$, the range of the field-of-view (FOV) covered by the DF is $\left[-\frac{H_{peak}}{G_x}, \frac{H_{peak}}{G_x}\right]$. The highest and the lowest FFP velocities are at the center and the edges of this FOV, respectively [1]. The safety limits, namely specific absorption rate (SAR) and magnetostimulation determine the optimal DF amplitude and frequency, hence its spatial coverage and the imaging speed [15, 16]. DF is created using an electromagnet, which is typically wound using a Litz wire. The reactive power of the DF coil is handled with impedance matching or tuning circuitry at a particular operating frequency [37]. Initially, the frequency and amplitude of the DF were around 25 kHz and 10-20 mT, respectively. Currently, the MPI systems generally apply a DF with a frequency range of 10 kHz to 100 kHz and an amplitude range of 10 mT to 100 mT [47]. Alternative to sinusoidal excitation, a pulsed MPI approach with an ideal square wave excitation has also been proposed [41].

2.2.3 Focus Field

FF is a low-frequency and high-amplitude magnetic field that shifts the FFR to positions that cannot be reached by DF alone [17, 18, 19]. The FFs are used to image a large fied-of-view (FOV) since the DF amplitude and frequency are constrained by hardware limitations and human safety concerns. SAR might exceed its regulatory limits and peripheral nerve stimulation (PNS) can happen when applying DFs in kHz range frequencies [15]. The frequency of the FF is in the range of a few Hz, i.e., much smaller than the DF frequency. The FFP is moved by the combination of the FF and DF. Similar to the DF, the FF can be generated using electromagnets.

2.2.4 Receive Coil

In MPI, a direct feedthrough signal is induced on the receive coil due to the time-varying DF. This direct feedthrough signal is a significant challenge in MPI, since its amplitude is several orders larger than the MNP signal amplitude, which makes discerning the MNP signal difficult during concurrent excitation and signal reception. Sinusoidal DFs are customarily chosen to contain the frequencies contaminated by the direct feedthrough. The receive coil typically has a gradiometric configuration to cancel out the direct feedthrough signal and reduce the interfering signals even if the background signals are dynamic during the measurement [48]. Alternative ways to negate the direct feedthrough signal include active/passive compensation and analog/digital filtering [49]. Typically, even if a gradiometric receive coil is utilized, the fundamental harmonic is considered to be contaminated and is filtered out.

2.2.5 Copper Shield

Formation of eddy currents on the surface of the permanent magnets that create the SF has to potential to induce interference signal on the receive coil. To avoid this issue, a hallow copper cylinder is placed in the bore of the scanner, outside the DF coil. The eddy currents are formed on the copper shield instead of the magnets, being in the opposite direction to the time-varying DF. The AC field amplitude that the permanent magnets experience is decreased, and the permanent magnets are effectively shielded [45].

2.3 Signal Equation

The position- and time-dependent total magnetic field applied to the MNPs consists of a constant gradient SF and a time-varying DF, which can be expressed

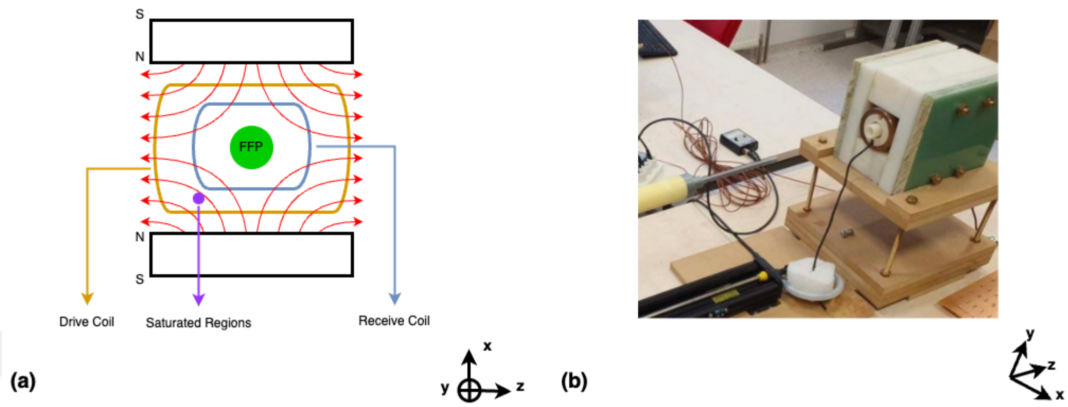

Figure 2.2: (a) A schematic of a conventional FFP MPI scanner configuration. Here, the red curves represent the SF generated by the permanent magnets, which are placed with North poles facing each other. The green circle represents the vicinity of the FFP. The MNPs at FFP are excited by the time-varying DF, generated by the drive coil. The receive coil records the response of the MNPs to the sinusoidal DF via induction. The spatial encoding is ensured as the induced signal originates from the MNPs within the vicinity of FFP. (b) Our in-house FFP Scanner.

as follows for the 1D case:

$$H(x,t) = H_d(t) + H_s(x) \tag{2.3}$$

where $H_d(t)$ is the DF and $H_s(x)$ is the SF. The DF is typically purely sinusoidal and can be expressed as:

$$H_d(t) = H_{peak} cos(2\pi f_d t) \tag{2.4}$$

where H_{peak} (T) is the peak field amplitude and f_d (Hz) is the DF frequency. Additionally, $H_s(x)$ can be expressed for 1D case as:

$$H_s(x) = -Gx \tag{2.5}$$

where $-G$ (T/m) is the SF gradient strength and x is the spatial position. The SF changes linearly as a function of position and the SF is specifically 0 at the vicinity of the FFP. The instantaneous location of the FFP, $x_s(t)$ (m) can be found by setting Equation (2.3) to 0 and solving for x, i.e.,

$$H(x,t) = H_d(t) - Gx_s(t) = 0 \tag{2.6}$$

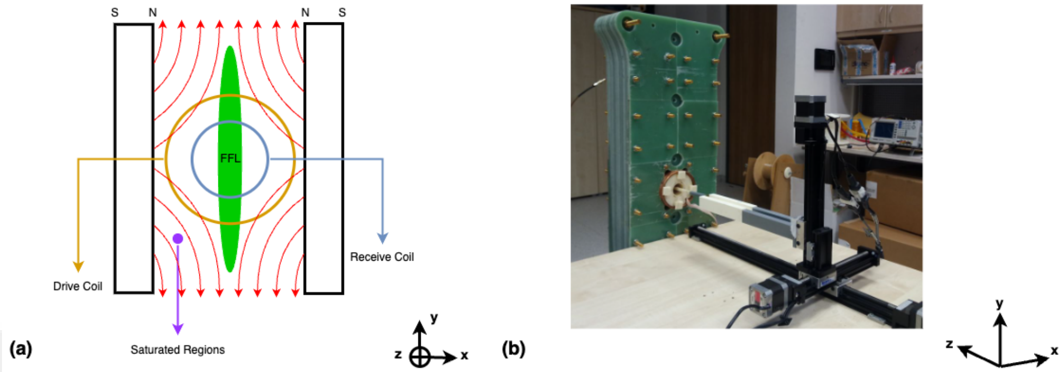

Figure 2.3: (a) A schematic of a conventional FFL MPI scanner configuration. Here, the red curves represent the SF generated by the permanent magnets. The green ellipsoid represents the vicinity of the FFL. The MNPs at FFL are excited by the time-varying DF, generated by the DF coils. The receive coil records the response of the MNPs to the sinusoidal DF via induction. The spatial encoding is ensured as the induced signal originates from the MNPs within the vicinity of FFL. (b) Our in-house FFL Scanner.

$$x_s(t) = \frac{H_d(t)}{G} \tag{2.7}$$

Then, Equation (2.3) can be reformulated as:

$$H(x,t) = G(x_s(t) - x). \tag{2.8}$$

The total magnetic field $H(x,t)$ changes the magnetization of the MNPs, which is modeled using the Langevin function as stated in Equation (2.1). The magnetization of a continuous 1D MNP distribution $\rho(x)$ can be explicitly obtained by replacing H in Equation (2.1) by the total magnetic field $H(x,t)$ in Equation (2.8):

$$M(x,t) = m\rho(x)\mathcal{L}(kG(x_s(t) - x)). \tag{2.9}$$

The electrical voltage signal induced on the receive coil can be expressed as the volume integral of the time derivative of $M(x,t)$. For the 1D case, the signal can be expressed as follows [22, 23]:

$$\begin{aligned} s_{adiab}(t) &= \int B_r \frac{\partial M(x,t)}{\partial t} dx \\ &= B_r \frac{\partial}{\partial t} \int M(x,t) dx \end{aligned} \tag{2.10}$$

where B_r is the sensitivity of the inductive receiver coil. By plugging Equation (2.9), we obtain:

$$\begin{aligned} s_{adiab}(t) &= B_r \frac{\partial}{\partial t} \int m\rho(x)\mathcal{L}(kG(x_s(t)-x))dx \\ &= B_r \frac{\partial}{\partial t}(m\rho(x) * \mathcal{L}(kGx))|_{x=x_s(t)} \\ &= B_r m\rho(x) * \dot{\mathcal{L}}(kGx)|_{x=x_s(t)} kG\dot{x}_s(t) \end{aligned} \tag{2.11}$$

where $\dot{x}_s(t)$ is the instantaneous FFP velocity.

2.4 Image Reconstruction Methods

System function reconstruction (SFR) and X-space reconstruction are the two main image reconstruction methods commonly employed in MPI. SFR involves a system matrix (SM), which explains the linear relation between the received signal and the spatial concentration of MNPs at a given location. In X-space image reconstruction obtains the MPI image by performing a velocity compensation and gridding of the received signal at the instantaneous position of the FFP. These two methods are described in more details below.

2.4.1 System Function Reconstruction

SFR represents the overall MPI signal as a linear combination of signals from the voxels in the FOV. The SM describes the relationship between the induced MNP signal and the spatial distribution of MNP concentration. Measurement-based methods, sparse recovery methods, and model-based methods are commonly utilized approaches to obtain the abovementioned linear mapping [50]. Establishing a factual physical model is a struggle due to the complexity of the environmental factors and and magnetization response of the MNPs. Previously, a model-based method was previously presented that produces SMs by utilization of a signal chain model [51]. Afterwards, the model-based approach for obtaining the SM is validated using 2D data [52]. Currently, the most accurate method is considered to be the measurement-based SM, which involves a calibration scan where the response of a point source MNP is collected at every voxel locations within the FOV using any type of FFP trajectory, which is depicted in Figure 2.4. The SM is constructed by placing the Fourier transform of the recorded signal at each voxel position in to the corresponding columns of the matrix [20].

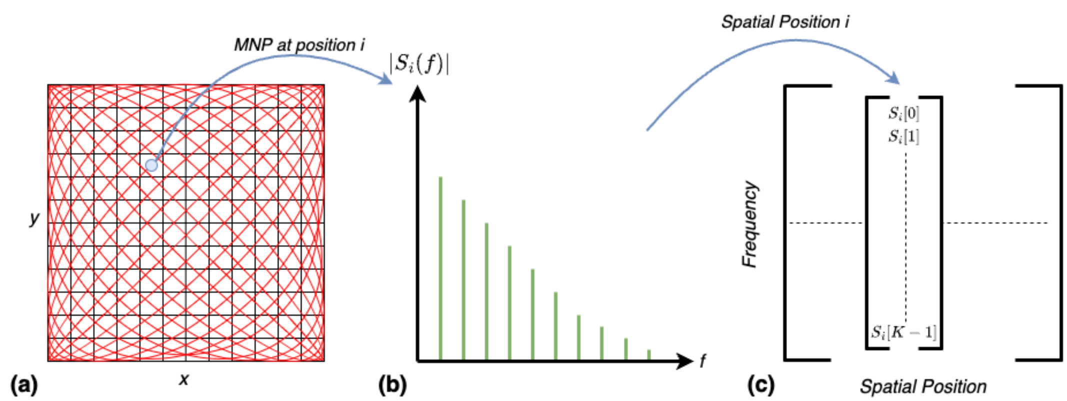

Figure 2.4: The calibration scan to obtain the SM. (a) The MPI signal of a point source MNP placed at the i^{th} voxel position is obtained. The curve indicated the FFP trajectory. (b) The Fourier Transform is applied to the received signal, (c) which is inserted into the i^{th} column of the SM.

A high-resolution image necessitates a lengthy calibration scan, as measuring the SM for a medium-sized image of 34×28×20 may take up to six hours [5, 53]. Sparse recovery methods that construct a fully-sampled SM from undersampled calibration scans have been proposed to alleviate the calibration time burden. In 2013, the number of calibration scans were reduced by a compressed sensing reconstruction method that exploits the fact that SMs have sparsity when basis transformations are applied to them. Some of these transformations include the discrete Fourier transform, discrete cosine transform, and discrete Chebyshev transform [53]. Later, a method was presented for compressing the SM further by taking advantage of the SM symmetry [54]. In addition, acquiring the SM using a coded calibration scene instead of a point source MNP was proposed to improve the both the SM and quality of the reconstructed image with the same experimental parameters, i.e., noise and sampling rate [55].

After obtaining the SM, the response of the spatial concentration of MNPs is recorded as a voltage signal applying the same FFP trajectory used during calibration. The linear relationship between the desired MNP concentration and the recorded voltage response signal can be described with the following:

$$\mathbf{u} = \mathbf{S}\mathbf{c} \tag{2.12}$$

where $\mathbf{S}$ is the SM, $\mathbf{u}$ is the Fourier transform of the received voltage vector during imaging, and $\mathbf{c}$ is the MNP concentration vector at all voxel positions within the FOV.

The desired MPI image vector $\mathbf{c}$ can be obtained by solving the equation (2.12). Typically, the inverse problem has an ill-posed nature, the reconstruction is improved by employing a type of regularization, most commonly Tikhonov, [52]. Singular value decomposition (SVD) and Cholesky decomposition are the most generally used direct methods to solve the linear equation. Although having advantages, such as SVD being able to tune the regularization parameter easily, the direct methods are impractical, especially for 3D MPI, because of their large memory requirement since the SM must be stored entirely to solve regularized linear equation [50]. Necessitating smaller memory and producing less computational effort, the regularized linear equation is widely solved by iterative methods such as Kaczmarz and the conjugate gradient method [50]. Alternatively, optimization methods such as Alternating Direction Method of Multipliers (ADMM) are also utilized for solving the problem via constrained convex optimization [56].

2.4.2 X-space Reconstruction

X-space reconstruction can accomplish reconstruction directly and faster, requiring no calibration scans. The received voltage signal is a sampled version of the desired MPI image at the instantaneous position of the FFP [50]. The reconstruction is done by appointing the speed-compensated received signal to the instantaneous FFP position. For the 1D case, the MPI image can be expressed in terms of the MNP concentration $\rho(x)$ from Equation (2.11):

$$\hat{\rho}(x) = \frac{s_{adiab}(t)}{B_r m k G \dot{x}_s(t)} \tag{2.13}$$

$$= \rho(x) * h(x)|_{x=x_s(t)} \tag{2.14}$$

$$= \rho(x) * \dot{\mathcal{L}}(kGx)|_{x=x_s(t)}. \tag{2.15}$$

Equation (2.15) formulates the MPI image as a convolution of the MNP concentration $\rho(x)$ and the point spread function (PSF) of the imaging system. The 1D PSF, $h(x) = \dot{\mathcal{L}}(kGx)$, is dependent on the MNP characteristics (due to parameter k) and the MPI system (due to parameter G) and causes a blurring in the MPI image.

X-space reconstruction technique was extended from 1D to 3D by proving that multidimensional MPI can be approximated as a linear shift-invariant system and deriving the PSF for multidimensional MPI [23]. While the equations for multidimensional x-space image equation are significantly more complicated, the derivation steps are similar to those for the 1D case.

The conventional x-space reconstruction forms the image by performing a speed compensation to the received signal and mapping it to the instantaneous position of the FFP [22, 23]. In MPI, human safety and hardware concerns limit the size of the region that the DF alone can cover. Therefore, multiple smaller partial FOVs (pFOVs) must be employed to cover the entire FOV. The separately processed pFOV images are combined to form the complete MPI image.

A drawback of x-space reconstruction is that the PSF of the imaging system blurs the reconstructed image. If the PSF is known or measured, deconvolution can be applied to improve image resolution. Another drawback of x-space reconstruction is that it assumes the MNP signals are adiabatic and models the MNP magnetization using the Langevin model. Ignoring the relaxation behavior of MNPs can lead to additional blurring and artifacts in the reconstructed images [50].

2.4.2.1 Partial FOV Center Imaging

Partial FOV Center Imaging (PCI) is a robust x-space reconstruction technique proposed to alleviate the susceptibility to harmonic interferences. The pFOV processing steps of standard x-space reconstruction can be easily affected by conditions where the receive signal is non-ideal, such as the cases where harmonic interference, noise, and relaxation effects are present [49]. The fundamental harmonic filtered to eliminate direct feedthrough signal is recovered during x-space reconstruction by enforcing smoothness and non-negativity [6, 49]. If there is a signal at higher harmonics induced by the non-idealities and/or interferences in the imaging system, the filtering out the fundamental harmonic is no longer sufficient. In practice, higher harmonic interferences are solved by taking a separate background measurement before and/or after the experiment and subtracting it from the received signal. However, for cases where the interferences have comparable levels to the MNP signal or there is a drift in the imaging system, the background cancellation cannot remove the interferences entirely and correctly [49].

PCI handles processing each pFOV in a considerably simplified manner by constructing the raw image of the total FOV by assigning the MNP signal directly to the center locations of the pFOVs. Then, the MPI image is obtained by deconvolving the raw image with a known, compact kernel. The shape of the deconvolution kernel depends on nothing but the size of the pFOVs, being independent of the other imaging parameters [49]. We can define the center of all pFOVs within the total FOV as:

$$x_s(t)|_{t=t_{0j}} = x_{0j}, \text{ for } j = 1, ..., N \tag{2.16}$$

where x_{0j} is the center position of the j^{th} pFOV, t_{0j} is the time instant when the FFP is at x_{0j}, and N is the total number of pFOVs. In PCI, the raw image is obtained by sampling the MNP signal $s(t)$ at the center of each pFOV:

$$\begin{aligned} \hat{\rho}_0(x_{0j}) &= s(t)|_{t=t_{0j}} && (2.17) \\ &= a\dot{x}_s(t_{0j})\hat{\rho}(x_{0j}) && (2.18) \\ &= \beta_0\hat{\rho}(x_{0j}) \text{ for } j = 1, ..., N. && (2.19) \end{aligned}$$

Here, $a = B_r mkG$ is a constant. The FFP velocity can be regarded to be identical at all pFOV centers since it is determined by the DF, which makes $\beta_0 = a\dot{x}_s(t_{0j})$ a constant for all N pFOVs [49]. It is important to note that $\hat{\rho}_0(x)$ does not contain the fundamental frequency due to direct feedthrough filtering. The lost first harmonic for a pFOV, which was shown to be a DC term [6, 20], can be formulated via a convolution for stepped focus fields [57]. This formulation is also valid for slowly varying focus fields. Accordingly, for the j^{th} pFOV:

$$\hat{\rho}_{dc}(x_{0j}) = \frac{4}{\pi W}\left(\hat{\rho}(x) * \sqrt{1-\left(\frac{2x}{W}\right)^2}\right)\Bigg|_{x=x_{0j}} \tag{2.20}$$

where W is the extent of each pFOV. The raw image at x_{0j} can be rewritten by taking the lost DC term into account, using Equations (2.19) and (2.20):

$$\tilde{\rho}_0(x_{0j}) = \beta_0(\hat{\rho}(x_{0j}) - \hat{\rho}_{dc}(x_{0j})) \tag{2.21}$$

$$= \beta_0\left(\hat{\rho}(x) * \left(\delta(x) - \frac{4}{\pi W}\sqrt{1-\left(\frac{2x}{W}\right)^2}\right)\right)\Bigg|_{x=x_{0j}} \tag{2.22}$$

$$\tag{2.23}$$

This relation is valid at the centers of all N pFOVs. A total raw image can be written as a convolution of the ideal image with a fully known compact kernel with full width W:

$$\tilde{\rho}_0(x) = \hat{\rho}(x) * h_0(x) \tag{2.24}$$

where

$$h_0(x) = \beta_0\left(\delta(x) - \frac{4}{\pi W}\sqrt{1-\left(\frac{2x}{W}\right)^2}\right) \tag{2.25}$$

Finally, the desired MPI image $\hat{\rho}(x)$ can be obtained by performing a deconvolution to $\tilde{\rho}_0(x)$ with $h_0(x)$, i.e.,

$$\hat{\rho}(x) = \tilde{\rho}_0(x) *^{-1} h_0(x). \tag{2.26}$$

For all harmonics, the MPI harmonic image basis, which consists of Chebyshev polynomials of the second kind [6, 20], varies relatively slowly near the centers of the pFOV compared to the edges, making the pFOV centers robust against harmonic interference effects, conversely making the edges more susceptible to the mentioned interferences [49]. Therefore using the signals solely at pFOV centers makes PCI reconstruction robust against harmonic interference effects.

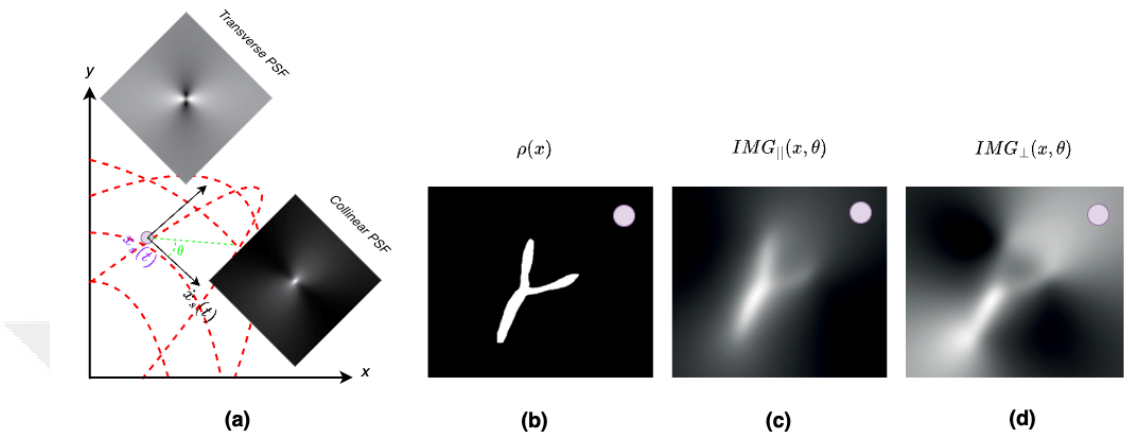

Figure 2.5: (a) The PSFs in collinear and transverse directions, aligned with the instantaneous velocity vector of the FFP by being revolved at an angle θ. Here, a portion of a Lissajous trajectory is shown in x-y plane. (b) The spatial concentration of MNPs. (c) The collinear image obtained by convolving the collinear PSF with the MNP distribution in space and (d) the transverse image obtained by convolving the transverse PSF with the MNP distribution in space. Figure adapted from [58].

2.4.2.2 Gridding Reconstruction for Non-Cartesian X-space

This technique expands x-space reconstruction to more complex multi-dimensional trajectories while still employing speed compensation and the signal assignment onto instantaneous FFP position, the operations essential in the x-space reconstruction [58].

In 3D x-space MPI theory, two vectors, one collinear and the other transverse to the FFP velocity vector, constitute a reference frame on which the images are produced [23]. The collinear image, depicted in Figure 2.5(c), created by convolving the collinear PSF, depicted in Figure 2.5(a), with the MNP distribution in Figure 2.5(b) [58], has higher resolution and higher image quality than the transverse image, depicted in Figure 2.5(d), created by convolving the transverse PSF, depicted in Figure 2.5(a), with the MNP distribution in Figure 2.5(b). For 1D DF, the axis of the receive coil is aligned with the speed vector of the FFP to exclusively obtain the collinear component of the MPI image. For the cases of 2D or 3D DFs, the collinear MPI image can be obtained by utilizing multiple receive coils to record the MNP signal and forming a virtual receive coil that is aligned with the instantaneous FFP speed vector by combining their signals accordingly [58]. The following paragraphs describe this procedure for the case of 2D DFs.

The proposed gridding reconstruction extracts the collinear component of the image from the received signals in x- and y-directions. The received MNP signals induced on two receive coils placed along physical x- and y-directions for a 2D FFP trajectory in x-y plane can be expressed as [58]:

$$s_x(t) = B_{r,x} mk \|\dot{\mathbf{x}}_s(t)\| \{IMG_{\parallel}(\mathbf{x}_s(t), \theta(t)) cos(\theta(t)) - IMG_{\perp}(\mathbf{x}_s(t), \theta(t)) sin(\theta(t))\} \tag{2.27}$$

and

$$s_y(t) = B_{r,y} mk \|\dot{\mathbf{x}}_s(t)\| \{IMG_{\parallel}(\mathbf{x}_s(t), \theta(t)) sin(\theta(t)) + IMG_{\perp}(\mathbf{x}_s(t), \theta(t)) cos(\theta(t))\} \tag{2.28}$$

where $B_{r,x}$ and $B_{r,y}$ are the receive coil sensitivities, $\mathbf{x}_s(t)$ and $\dot{\mathbf{x}}_s(t)$ are the instantaneous position and velocity vectors, $\theta(t)$ is the angle of the FFP speed vector with respect to the x-axis. The collinear and transverse images can be denoted as a convolution operation between the corresponding PSFs and the MNP distribution in space, i.e.,

$$IMG_{\parallel}(\mathbf{x}_s(t), \theta(t)) = \rho(\mathbf{x}) * h_{\parallel}(\mathbf{x}, \theta(t))|_{\mathbf{x}=\mathbf{x}_s(t)} \tag{2.29}$$

$$IMG_{\perp}(\mathbf{x}_s(t), \theta(t)) = \rho(\mathbf{x}) * h_{\perp}(\mathbf{x}, \theta(t))|_{\mathbf{x}=\mathbf{x}_s(t)}. \tag{2.30}$$

Here, $h_{\parallel}(\mathbf{x}, \theta(t))$ and $h_{\perp}(\mathbf{x}, \theta(t))$ are the collinear and transverse PSFs, respectively, and $\mathbf{x}$ is the position vector. As shown in Figure 2.5(a), these PSFs are rotated by an angle θ to be in the same direction as the FFP velocity vector at time instant t. Figure 2.5(c) and (d) show the collinear and transverse images formed by convolving the MNP distribution with the corresponding PSFs, respectively. The resolution and quality of the collinear image is better than the transverse image [58].

The gridding reconstruction aims to reformulate the collinear image in terms of the received signals $s_x(t)$ and $s_y(t)$. The signal for a virtual receive coil in line with the FFP velocity vector can be expressed as [59]:

$$s_v(t) = \frac{s_x(t)}{B_{r,x}} cos(\theta(t)) + \frac{s_y(t)}{B_{r,y}} sin(\theta(t)) \tag{2.31}$$

$$= mk\|\dot{\mathbf{x}}_s(t)\| \; IMG_{\|}(\mathbf{x}_s(t), \theta(t)). \tag{2.32}$$

The resulting image for a virtual coil after speed compensation can be expressed as:

$$IMG_v(\mathbf{x}_s(t)) = \frac{s_v(t)}{\|\dot{\mathbf{x}}_s(t)\|} = \alpha IMG_{\|}(\mathbf{x}_s(t), \theta(t)) \tag{2.33}$$

where $\alpha = mk$ is a constant. The proposed technique only grids the collinear component of the signal to improve image quality.

The inspiration for this technique is the gridding algorithms in MRI, which convolves the data points on a non-Cartesian k-space trajectory with a kernel, applies sampling operation to the convolved data samples and grids the samples onto a Cartesian k-space grid. The MRI image is reconstructed after density compensation of the scanning trajectory [58]. The gridding reconstruction for non-Cartesian x-space MPI proposes a gridding algorithm in image domain since the signal equation is directly expressed in image domain:

$$\widehat{IMG(\mathbf{x})} = \frac{\widehat{IMG}_{init}(\mathbf{x})}{\hat{d}_s(\mathbf{x})} = \frac{((IMG(\mathbf{x})s(\mathbf{x})) * c(\mathbf{x})) \cdot \mathrm{III}(\frac{\mathbf{x}}{\Delta x})}{(s(\mathbf{x}) * c(\mathbf{x})) \cdot \mathrm{III}(\frac{\mathbf{x}}{\Delta x})} \tag{2.34}$$

where

$$s(\mathbf{x}) = \sum_{i=1}^{N_s} \delta(\mathbf{x} - \mathbf{x}_i) \tag{2.35}$$

$$IMG(\mathbf{x}_i) = IMG_v(\mathbf{x}_s(t_i)), \text{ i} = 1, ..., N_s. \tag{2.36}$$

Here, $IMG(\mathbf{x})$ refers to the ideal image to be reconstructed, sampled at FFP locations on the trajectory, $s(\mathbf{x})$ is a non-Cartesian sampling function with impulses placed at sampled FFP positions, $\mathbf{x}_i = \mathbf{x}_s(t_i)$ is the FFP position at time instant t_i, $\mathrm{III}(\frac{\mathbf{x}}{\Delta x})$ is a 2D Comb function for re-sampling onto the Cartesian Grid, $c(\mathbf{x})$ is the gridding kernel in image domain which is a Kaiser-Bessel window, a common choice for MRI gridding algorithms [58]. Also, Δx is the resolution of the Cartesian grid, i.e., the distance between two adjacent points on the grid.

To achieve a high-quality reconstruction, the acquired data must be spread to all pixels in the Cartesian grid and the parameters of the kernel, namely the kernel width and image size must be tuned deliberately [58].

2.5 Relaxation Mapping via Color MPI

2.5.1 Relaxation Behavior of MNPs

The signal equation for MPI in Equation (2.11) is formulated under the assumption that the magnetization of the MNPs aligns instantaneously with the time-varying magnetic field. In practice, there is a delay in the alignment due to the relaxation of the MNPs. Two distinct mechanisms, as depicted in Figure 2.6(a), contribute to the relaxation process under an oscillating DF [60]: Néel relaxation and Brownian relaxation.

1. In Néel relaxation, the orientation of the magnetic moments of the MNPs changes internally. The time constant for the Néel relaxation process is given as:

$$\tau_N = \tau_0 \frac{\sqrt{\pi} e^{\sigma}}{2\sqrt{\sigma}} \tag{2.37}$$

   where

$$\sigma = \frac{K V_c}{k_B T}. \tag{2.38}$$

   In Equation (2.37), τ_0 is the attempt time [61], K is the anisotropy constant of the MNPs, and σ refers to the ratio of anisotropic and thermal energies of the MNP.

2. In Brownian relaxation, the MNPs physically rotate to align their magnetic moment with the time-varying external magnetic field. The time constant associated with the Brownian relaxation is given as:

$$\tau_B = \frac{3 \nu V_h}{k_B T} \tag{2.39}$$

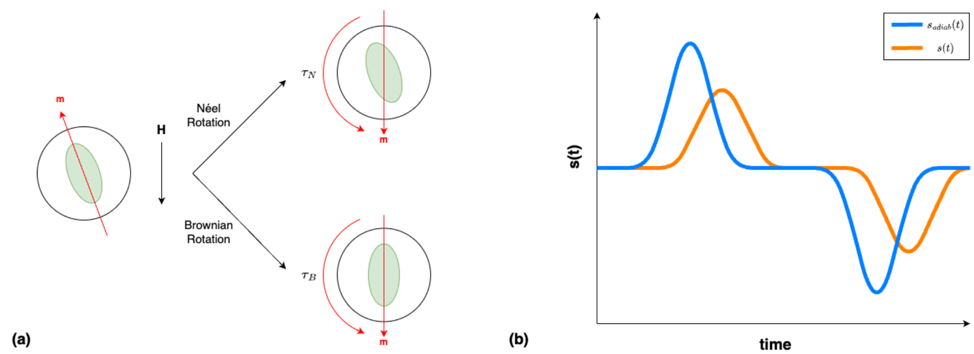

Figure 2.6: (a) The Brownian and Néel relaxation mechanisms. The magnetic moment of the MNP is illustrated with a red arrow, its magnetic core with a green ellipse and the coating around the core with a black circle. (b) The effects of the relaxation on the MPI signal. Compared to the ideal adiabatic signal, $s_{adiab}(t)$, a delay and a decrease in the signal amplitude can be observed in the signal with relaxation, $s(t)$.

where ν is the viscosity of the environment, and V_h is the hydrodynamic volume of the MNPs.

These two mechanisms work in parallel, and result in a net effective time constant that is typically expressed as [61]:

$$\tau_{eff} = \left(\frac{1}{\tau_N} + \frac{1}{\tau_B} \right)^{-1} \tag{2.40}$$

It is important to note that the relaxation mechanisms in MPI work differently than the relation in Equation (2.40) since the Brownian and Néel relaxation mechanisms explain the behavior of MNPs under zero-field, i.e., when an applied DC field is suddenly removed [62]. In the case of MPI, however, a time-varying DF is applied to generate the MNP response. The relaxation of MNPs shows different properties due to these overlapping magnetic fields, and can be modeled as a Debye process:

$$s(t) = s_{adiab}(t) * r_\tau(t) \tag{2.41}$$

where

$$r_\tau(t) = \frac{1}{\tau} e^{-\frac{t}{\tau}} u(t). \tag{2.42}$$

In Equation (2.41), $s(t)$ is the signal with relaxation, $s_{adiab}(t)$ is the ideal signal as described in Equation (2.11), $*$ denotes convolution over t, and $r_\tau(t)$ is the relaxation kernel. In addition, τ is the effective relaxation time constant of the MNP in seconds and $u(t)$ is the Heaviside unit step function [24]. As shown in Figure 2.6(b), relaxation process induces blurring and lowers the SNR of the ideal adiabatic signal given in Equation (2.11).

2.5.2 Time Constant Estimation via TAURUS

The adiabatic signal, $s_{adiab}(t)$, features a mirror symmetry that is valid for every type of MNP and distribution in space, for the cases where the signal is acquired with a back-and-forth FFP trajectory [28, 63]. To express the mirror symmetry in mathematical form, the negative and positive signals can be defined as the half-cycle signals acquired during the back and forth FFP movement, respectively. The mirror symmetry in the adiabatic signal can be expressed as:

$$s_{pos,adiab}(t) = -s_{neg,adiab}(-t) = s_{half} \tag{2.43}$$

The relaxation mechanisms distort this mirror symmetry. Using Equations (2.41) and (2.43), we can express the negative and positive signals with relaxation as:

$$s_{pos}(t) = s_{half}(t) * r_\tau(t) \tag{2.44}$$

$$s_{neg}(t) = -s_{half}(-t) * r_\tau(t) \tag{2.45}$$

Taking the Fourier transform of s_{pos} and s_{neg} yield:

$$S_{pos}(f) = \mathcal{F}\{s_{pos}(t)\} = S_{half} R_\tau(f) \tag{2.46}$$

$$S_{neg}(f) = \mathcal{F}\{s_{neg}(t)\} = -S^*_{half} R_\tau(f) \tag{2.47}$$

$$R_\tau(f) = \mathcal{F}\{r_\tau(t)\} = \frac{1}{1 + i2\pi f\tau} \tag{2.48}$$

where $\mathcal{F}$ is the Fourier transformation operation and superscript * denotes complex conjugation. Using the Fourier transform of s_{pos} and s_{neg}, τ can be computed in the frequency domain as follows [28, 63]:

$$\tau(f) = \frac{S^*_{pos}(f) + S_{neg}(f)}{i2\pi f(S^*_{pos}(f) - S_{neg}(f))}. \tag{2.49}$$

The computed relaxation time constant $\tau(f)$ should be independent of frequency in the ideal case. Nevertheless, the deviations from the relaxation model in Equation (2.41) or noise in the system may induce frequency dependency [64]. A weighted average of $\tau(f)$ is computed with the magnitude spectrum $|S_{pos}(f)|$ as weights [63]. The adiabatic signal, $s_{adiab}(t)$ can be obtained by deconvolving $s(t)$ with $r_\tau(t)$ [64].

2.5.3 Rapid TAURUS

The mirror symmetry in the adiabatic signal, $s_{adiab}(t)$, is distorted for trajectories with time-varying FFs. The center of the pFOV shifts, which causes non-symmetrical FFP motion around the pFOV center. Additionally, the mirror symmetry is further altered by different trajectory speeds of the positive and negative signals. The slew rate of the FF causes a delay between the positive and negative signals and a magnitude disparity. The Rapid TAURUS technique proposes a slew rate correction to restore the mirror symmetry in $s_{adiab}(t)$ as follows [64]:

$$S_{pos,c}(f) = S_{pos,d}(f) \tag{2.50}$$

$$S_{neg,c}(f) = S_{neg,d}(f)e^{i2\pi\Delta tf}\alpha. \tag{2.51}$$

Here, $S_{pos,c}$ and $S_{pos,c}$ are the corrected positive and negative signals, respectively, and $S_{pos,d}$ and $S_{neg,d}$ are the positive and negative signals distorted due to time-varying FFs. Additionally, α is the amplitude scaling, which is the ratio of the FFP velocities at t_0 and $t_0 + T/2 + \Delta t$, and given as:

$$\alpha = \frac{|B_p 2\pi f_d cos(2\pi f_d \Delta t) + R_{s,z}|}{|-B_p 2\pi f_d + R_{s,z}|}. \tag{2.52}$$

Here, $T = 1/f_d$ is the period of the drive field and t_0 is the time point at which the FFP speed is maximum in the first negative half-cycle. Lastly, Δt is the FF-induced time shift, given approximately as:

$$\Delta t = \frac{-R_{s,z}}{2f_d(B_p 2\pi f_d + R_{s,z})}. \tag{2.53}$$

For Equations (2.52) and (2.53), $R_{s,z}$ is the slew rate of the FF along z-direction, B_p and f_d are the peak amplitude and the frequency of the DF, respectively.

Equation (2.49) can be used with the corrected signals, $S_{pos,c}$ and $S_{pos,c}$, to obtain SR-corrected estimation in frequency domain [64]:

$$\tau(f) = \frac{S^*_{pos,c}(f) + S_{neg,c}(f)}{i2\pi f(S^*_{pos,c}(f) - S_{neg,c}(f))}. \tag{2.54}$$

Note that when $\Delta t = 0$, which corresponds to the case of zero slew rate, this equation converges to Equation (2.49).

Chapter 3

Preclinical Arbitrary Waveform FFL MPI Scanner

Parts of this chapter are based on the following publications:

B. Alyuz, M.T. Arslan, M. Utkur and E.U. Saritas, "An Arbitrary Waveform MPI Scanner", International Journal on Magnetic Particle Imaging, 8(1 Suppl 1):203077, 2022.

B. Alyuz, M.T. Arslan, M. Utkur and E.U. Saritas, "Single-Pass Relaxation Mapping at Multiple Frequencies using an Arbitrary Waveform MPI Scanner", International Journal on Magnetic Particle Imaging, 9(1 Suppl 1):2303075, 2023.

3.1 Introduction

Magnetic particle imaging (MPI) scanners utilize drive fields (DF) to excite magnetic nanoparticles (MNP) and image their spatial distribution. Typical MPI scanners handle the reactive power on the drive coil via impedance matching circuitry tuned to a single resonant frequency. The necessity for such circuitry limits the flexibility of the imaging system, restricting it to a particular operating frequency. However, the optimal frequency may be different for functional imaging applications of MPI such as viscosity mapping or temperature mapping [31, 33].

Reducing the reactive power on the power amplifier is necessary to achieve DF amplitudes large enough to excite the MNPs. One method to reduce the reactive power for a wide bandwidth is miniaturizing the drive coil to reduce its inductance [38]. Reduced inductance eliminates the need for impedance matching, enabling arbitrary waveform (AW) characteristics. Previous studies achieved AW characteristics for magnetic particle spectrometer (MPS) and relaxometer setups [38, 39, 40]. Additionally, a small-scale field free line (FFL) MPI scanner was constructed by adding magnets to an AW relaxometer to enable pulsed excitation in MPI [41]. While employing small-scale coils is feasible for such setups, typical MPI scanners have considerably larger dimensions.

This chapter proposes an AW drive coil design to achieve AW characteristics in an MPI scanner. The proposed design utilizes Rutherford cable windings to achieve a 144-fold reduction in inductance compared to a standard drive coil. Low inductive reactance enables functionality in a wide range of frequencies without a need for impedance matching or tuning circuitry. Proof-of-concept results are demonstrated via imaging experiments on an FFL scanner with two distinct sinusoidal DF waveforms at 2.5 kHz and 5 kHz.

3.2 Arbitrary Waveform Drive Coil

To obviate the need for impedance matching at a specific DF frequency, we propose an AW drive coil that utilizes Rutherford cable windings. This design can considerably reduce the inductance of the drive coil and hence the reactive power that the power amplifier needs to supply. To form Rutherford cable windings, N_R Litz wires are twisted together to form a single cable with a rectangular cross-section, as illustrated in Figure 3.1(a). With this topology the number of windings is reduced to $N_L' = N_L/N_R$, where N_L is the number of regular windings with the wire of the same length [65].

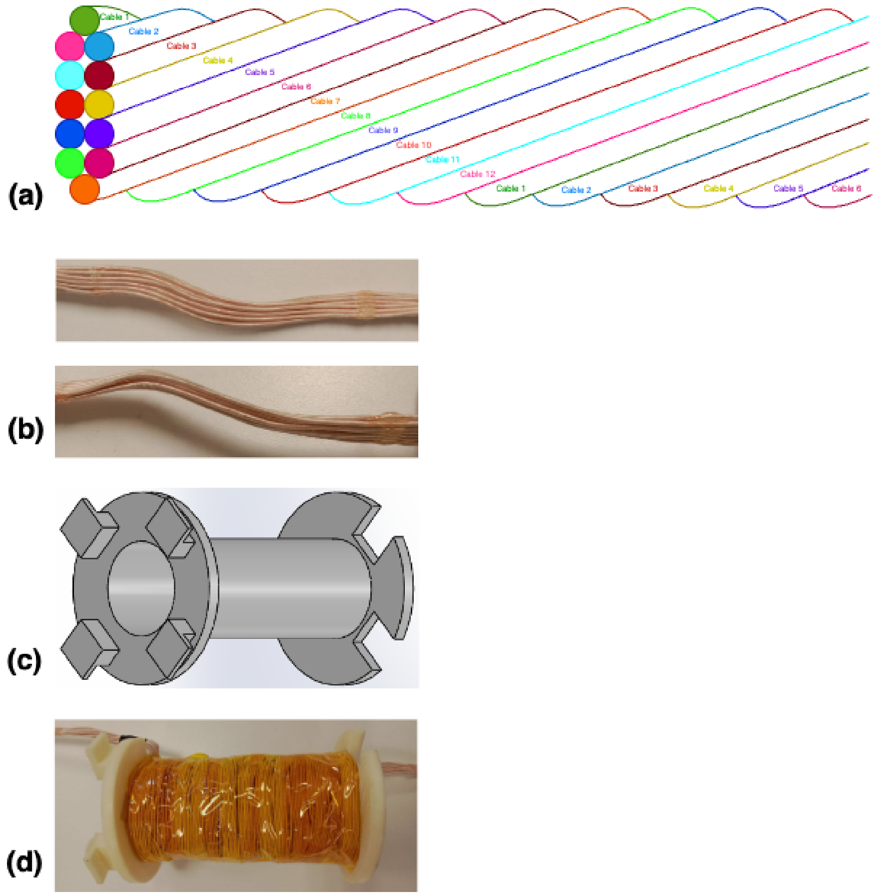

Figure 3.1: Rutherford cable windings and AW drive coil. (a) Rutherford cable winding technique for a Rutherford cable with 12 Litz wires, twisted together to form a 6×2 rectangular cross-section. (b) Rutherford cable windings prepared for our AW drive coil. Here, the number of windings in the Rutherford cable is chosen as 12. (c) The coil former for the constructed AW drive coil that includes 4 extensions that hold on to the copper shield to ensure accurate positioning. (d) The constructed AW drive coil.

Inductance of a coil for the case of regular windings can be expressed as:

$$L = A_L N_L^2 \tag{3.1}$$

where A_L is the inductance constant. In the case of using a Rutherford cable, there is a N_R^2-fold reduction in the coil inductance assuming A_L remains approximately the same, i.e.,

$$L' \approx A_L N_L'^2 = A_L \left(\frac{N_L}{N_R}\right)^2 = \frac{L}{N_R^2} \tag{3.2}$$

To generate the same magnetic field, the total current on the Rutherford cable should be equal to $I' = IN_R$, where I is the current on the wire in the case of regular windings. Therefore, the voltage on the coil can be expressed as:

$$V' = I'j\omega L' \approx IN_R j\omega \frac{L}{N_R^2} = \frac{V}{N_R}. \tag{3.3}$$

Here, $V = Ij\omega L$ is the voltage on the coil with regular windings. As seen in these relations, since the number of windings is reduced N_R-fold using a Rutherford cable, the inductance is reduced N_R^2-fold, and the voltage on the coil is reduced N_R-fold [65].

Table 3.1 lists the specifications of the AW drive coil, comparing it with a standard drive coil of identical diameter and length but with regular Litz wire windings. In our design, we chose N_R as 12. The Rutherford cable was prepared using 125/40 AWG Litz wires, twisted together to form a 6×2 rectangular cross-section, as shown in Figure 3.1(b). The inner diameter of the drive coil was 4.4 cm, with a length of 12 cm. The AW drive coil, shown in Figure 3.1(d), had 3 layers with 13 Rutherford cable windings per layer. The separation between the drive coil and the copper shield played a critical role in determining the number of layers, since the copper shield reduces the drive coil sensitivity as the separation gets smaller. For our in-house MPI scanner, 3 layers provided a favorable trade-off between high coil sensitivity and reduced coil inductance, achieving functionality in a wide range of frequencies within the hardware limits.

3.2.1 Simulations

The designed AW drive coil was simulated in COMSOL Multiphysics ®Version 5.5. There is no publicly available method to simulate Rutherford cable windings in COMSOL. Here, we utilized a 2D axisymmetric model, and simulated each 6×2 cross-section of the Rutherford cable as a single solid wire. The copper shield of our in-house MPI scanner was also incorporated into these simulations to account for the shielding effects. The goal of these simulations was to predict the coil performance in terms of coil sensitivity, inductance, and resistive heating. To

Table 3.1: Comparison of coil specifications for a standard drive coil and an AW drive coil

	Simulated Standard Drive Coil	**Simulated AW Drive Coil**	**Measured AW Drive Coil**
Inner Diameter	44 mm	44 mm	44 mm
Coil Length	120 mm	120 mm	120 mm
# of Layers	6	3	3
Inductance	3.56 mH	24.75 µH	23.87 µH
DC Resistance	1.14 Ω	7.7 mΩ	32.03 mΩ
Coil Sensitivity at 8 kHz	3.28 mT/A	0.274 mT/A	0.268 mT/A
Voltage at 8 kHz**,** 10 mT	386.8 V	32.3 V	44.8 V
Voltage at 5 kHz**,** 15 mT	363.62 V	30.3 V	42.0 V

this end, a Frequency-Transient study was utilized to compute the temperature changes over time and the electromagnetic field distribution as a function of operating frequency. Electromagnetic field distribution and temperature changes were simulated using Magnetic Fields and Heat Transfer in Solids interfaces, respectively. For the heating simulations, the room temperature was taken as 25 °C.

The coil sensitivity was simulated at 5 kHz and 8 kHz. The resistive heating was simulated at two different DF settings amplitude of 10 mT at 8 kHz and amplitude of 15 mT at 5 kHz. The duration of DF was chosen as 90 s, as it corresponded to the maximum scan time duration expected to be utilized during the experiments.

The results of coil sensitivity and resistive heating simulations are given in Fig. 3.2. The simulated temperature increase due to resistive heating remained negligible after continuously applying the DF at 8 kHz and 10 mT for 90 s. Similarly, the temperature increase remained low for DF at 5 kHz and 15 mT, as well. These results indicate that no external cooling is required.

As given in Table 3.1, the simulated AW drive coil achieves approximately 12-fold reduction in the required voltage when compared to the standard drive coil,

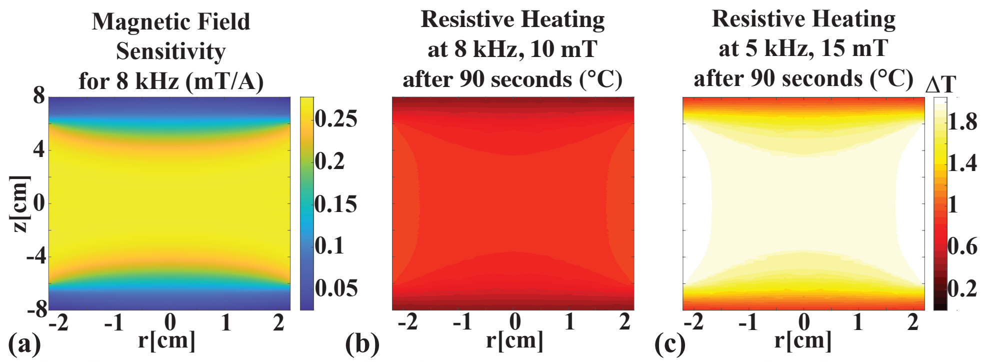

Figure 3.2: COMSOL simulation results for the AW drive coil. (a) The coil sensitivity at 8 kHz, and (b) the temperature change (ΔT) due to resistive heating after continuously applying the DF for 90 s at 8 kHz and 10 mT (c) and 5 kHz and 15 mT. In heating simulations, the room temperature was taken as 25 °C.

reducing it from 386.8 V to 32.3 V at 8 kHz and 10 mT. In addition, it achieves 144-fold reduction in the coil inductance when compared to the standard drive coil, reducing it from 3.56 mH to 24.75 µH. The Rutherford cable winding reduces both the DC resistance and the inductance, scaling down the required voltages. As a trade-off, the reduced coil sensitivity of the AW drive coil indicates higher current requirements, which creates a hardware limitation on the DF amplitude.

3.2.2 Measurements

Inductance and DC resistance measurements for the constructed AW drive coil was performed using an LCR meter (GW Instek LCR-8105G). The coil sensitivity was measured using a gaussmeter (Lakeshore 475 DSP) along the central line of the AW drive coil, while applying a DF at 8 kHz. The current through the drive coil was measured using a current probe (LFR 06/6/300, PEM). During these measurement, the drive coil was inside the copper shield, as the presence of the copper shield significantly affects the inductance and sensitivity of the drive coil. Then, the voltage for both DF settings were calculated using the measured inductance, DC resistance, and coil sensitivity.

As given in Table 3.1, the specifications for the simulated and measured AW

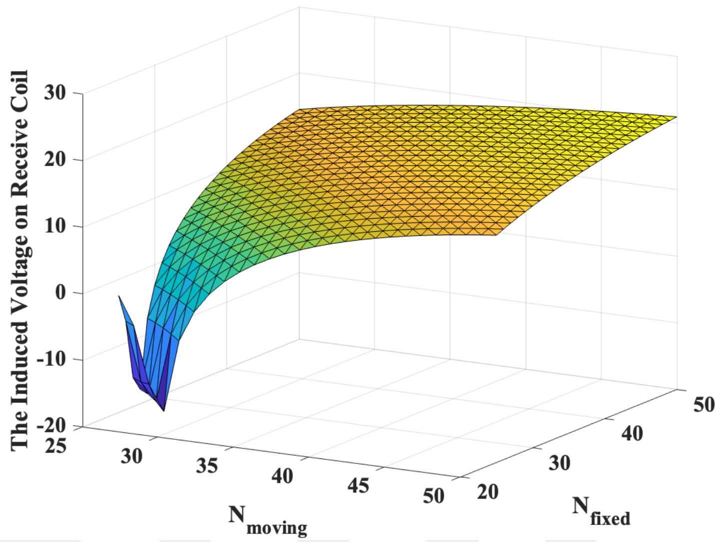

Figure 3.3: The surface plot of the simulated direct feedthrough voltage induced on the receive coil as a function of the number of turns in the moving and fixed part of the gradiometric receive coil.

drive coils match closely. The slight deviations may stem from the simulation approach for Rutherford cable winding, as well as the non-idealities in the cable and coil implementation.

3.3 Gradiometric Receive Coil

A receive coil was designed together with the AW DF coil. It had a three-section gradiometer geometry with 27, 50, and 31 turns for the fixed compensation, center receive, and tuning parts, respectively, achieving around 65 dB decoupling between drive and receive coils. The simulations were done using COMSOL Multiphysics ®Version 5.5. A 2D axisymmetric model was used to model the subcomponents of the AW MPI scanner utilizing the Magnetic Fields interface to simulate the direct feedthrough signal. The optimal number of turns for the fixed compensation and the tuning segment were found with grid search by employing Parametric Sweep study.

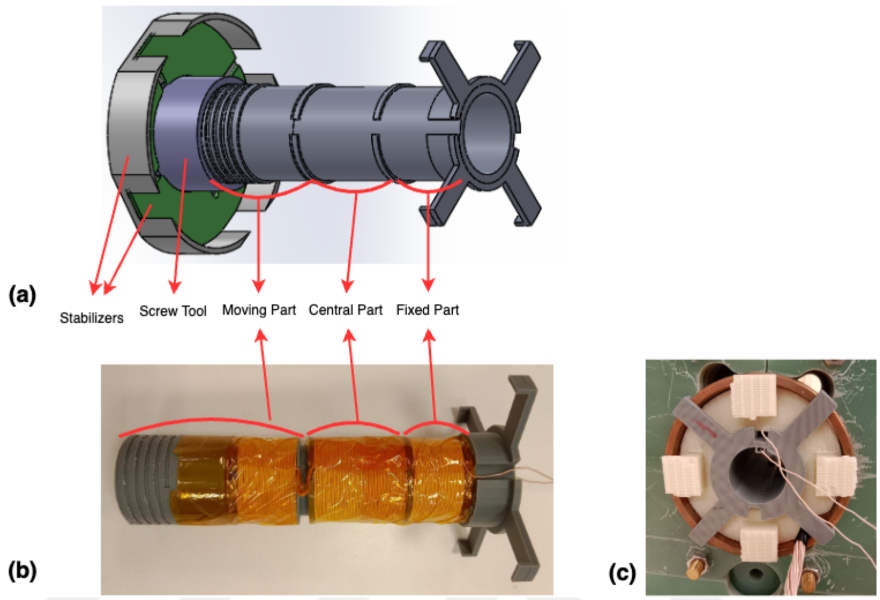

Figure 3.4: Implementation details of the gradiometric receive coil. (a) 3D design of the coil former. It featured a stable part that includes the fixed compensation and the central parts. The stable part had 4 extensions to hold on to copper shield to ensure accurate positioning. Additionally, the coil former for the moving part was separate. Lastly, the former design included a screw tool to enable fine tuning, stabilizers to make sure that the receive coil does not move laterally. All parts are marked with red arrows. (b) Constructed gradiometric receive coil. The fixed, central, and the moving parts are marked with red arrows. (c) The gradiometric receive coil inside the AW drive coil. Both feature extensions to hold on to the copper shield for stabilization and accurate positioning inside the MPI scanner.

The number of turns in the center part of the receive coil was chosen as 50 to maintain a homogeneous receive sensitivity profile ($> 90\%$ homogeneity) in a targeted 12.5 mm region at the scanner isocenter. Then, the induced voltage on the receive coil ($20log_{10}(|V_{induced}|)$) was simulated for varying number of turns in the fixed and the moving parts of the receive coil when the separation between the center and the moving part is 0. The range for the number of turns in the fixed and the moving parts was chosen as 25 to 50 turns. Figure 3.3 shows the results of the simulation, where configurations that significantly minimizes the induced voltage on receive coil are clearly visible. Accordingly, the ideal number of turns for the fixed compensation part was chosen as 27. The number of turns for the

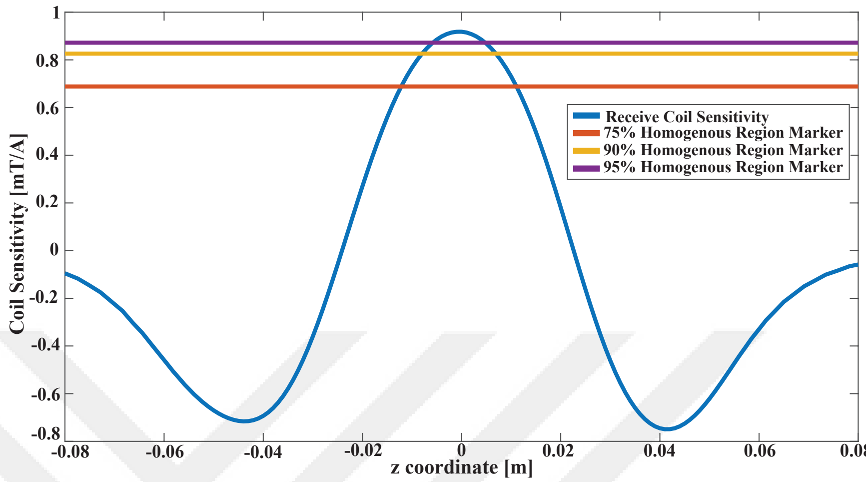

Figure 3.5: The simulated sensitivity profile of the gradiometric receive coil along the central z-axis.

moving compensation was increased to 31 to allow for an appropriate separation between the center and the moving parts for ideal tuning and minimization of the induced voltage on receive coil.

The designed coil had 27, 50 and 31 number of turns for the fixed, the central and the moving part, respectively. Figure 3.4(a) shows the 3D design of the coil former on which the receive coil was wound. The fixed and the central compensation parts were wound onto one part of the coil former design, while the moving part was wound onto a separate part to enable tuning. To ensure that the movement is only on one axis, a small rectangular part of the former for the fixed and central parts was left empty, while the corresponding part of the former for the moving part had a rectangular shaped extension. Figure 3.4(b)-(c) shows the constructed gradiometric receive coil and how it is attached to copper shield to ensure stabilization and accurate positioning inside the MPI scanner .

Figure 3.5 shows the sensitivity profile of the designed receive coil with 27, 50, and 31 turns in the fixed, center and moving compensation parts, respectively. Here, 75% homogenous region length is 23 mm, 90% homogenous region length is 14 mm and 95% homogenous region length is 10 mm.

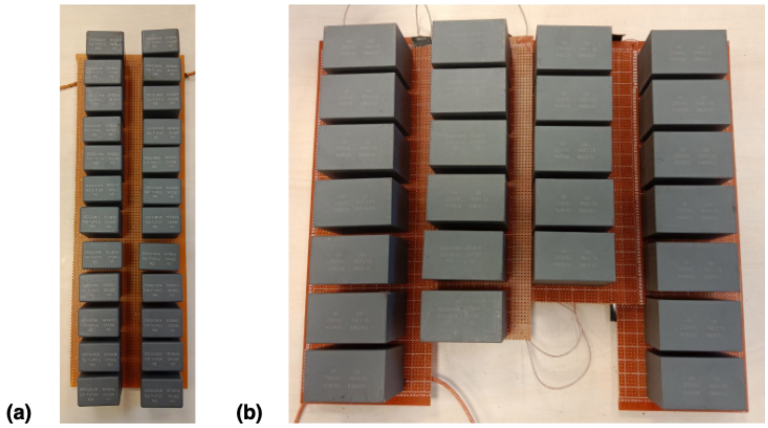

Figure 3.6: The constructed capacitor banks. (a) 2×12 capacitor bank with capacitance value of 30 µF. (b) 1×25 capacitor bank with capacitance value of 1000 µF.

3.4 Capacitor Banks

Capacitor arrays were designed to prevent a possible shift in the FFL position due to the presence of DC voltages at the output of the power amplifier. In total two capacitor arrays were designed: one array with a total capacitance of 30 µF and one array with a total capacitance of 1000 µF, as shown in Figure 3.6. Two different capacitance values were used since the capacitance values of the capacitor banks distort the applied DF waveform, and therefore affect the received signal. This especially becomes important for our application where DF waveforms at different frequencies are applied consecutively in a single scan. To simulate this effect, an LTSpice simulation was performed by drawing the circuit schematic of the imaging setup and observing the transmitted DF waveform.

In Figure 3.7, V_1 denotes the voltage source, supplying the circuit with the voltage signal that is required to generate the constructed DF waveform with two different DF settings, namely (8 kHz,10 mT) and (5 kHz,15 mT). L_{TX} and L_{RX} are the inductances of the drive coil and receive coil, respectively. Finally, $C_{DCBlock}$ is the capacitance of the capacitor bank to block out interference signals near DC. The simulation was performed for 4 periods of the DF waveform, with

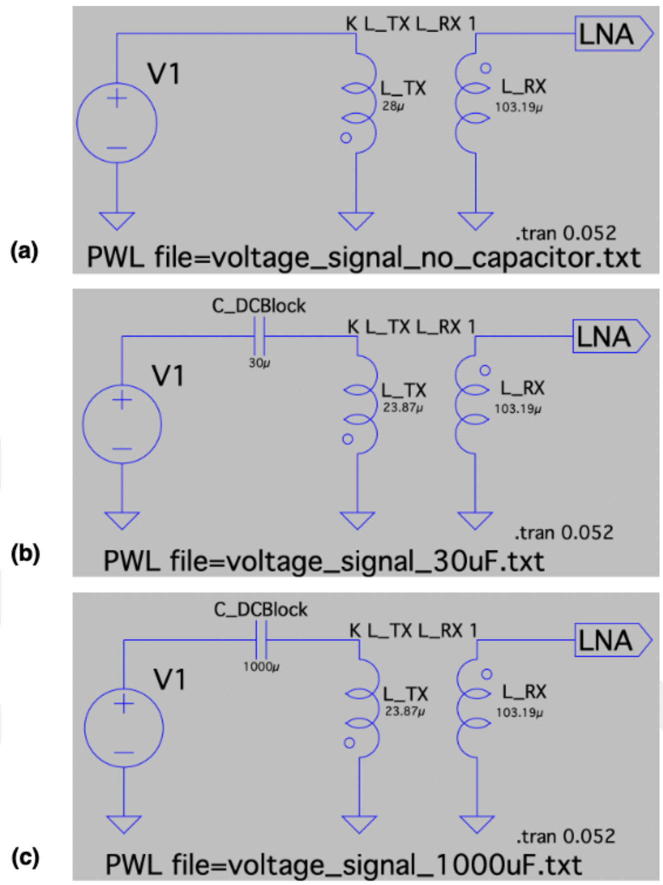

Figure 3.7: LTSpice circuit schematic of the imaging setup (a) without a capacitor bank, (b) with a 30 µF capacitor bank, and (c) with a 1000 µF capacitor bank.

each period consisting of 40 periods of a sinusoid at (8 kHz,10 mT) followed by 40 periods of a sinusoid at (5 kHz,15 mT). For the cases without and with capacitor banks, the voltage waveforms V_1 were created using MATLAB to ensure that the desired currents can be formed to generate the desired DF amplitudes. These waveforms were then used as voltage supply by utilizing piecewise linear function in LTSpice.

With LTSpice, the current on the drive coil was simulated, as shown in Figure 3.8. The effect of the capacitance of the bank on the transmitted DF waveform is evident in Figure 3.8. When there is no capacitor bank in the imaging setup, the current waveform on the AW drive coil is shown in Figure 3.8(a). When the capacitance value is small, i.e., 30 µF, the shape of the current waveform is significantly distorted, as depicted in Figure 3.8(b). The capacitor bank with 1000 µF

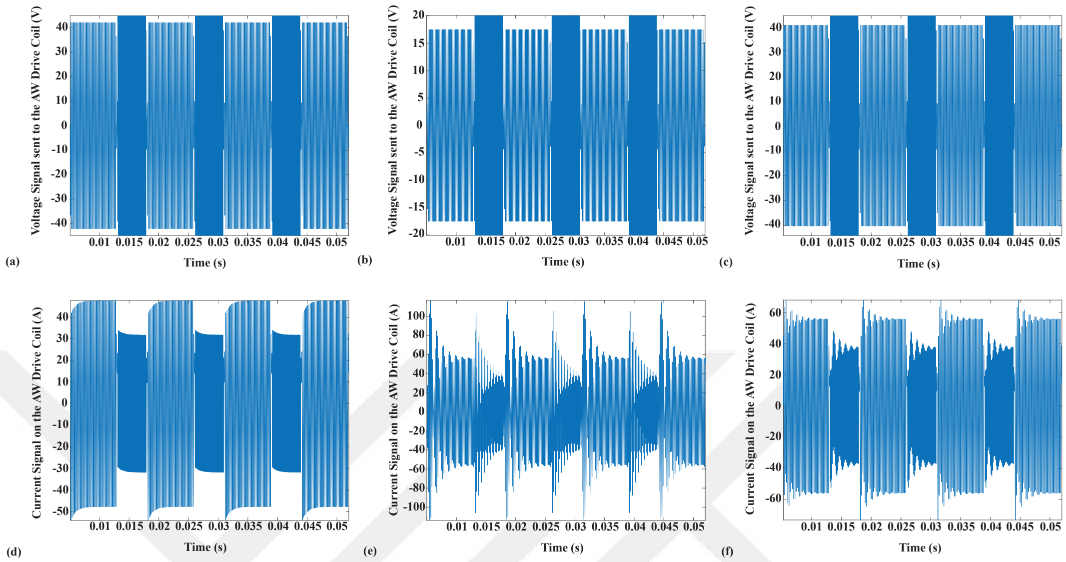

Figure 3.8: The voltage sent to the AW drive coil (a) without a capacitor bank in the imaging setup, (b) with a 30 µF capacitor bank, and (c) with a 1000 µF capacitor bank. The current on the AW drive coil (d) without a capacitor bank in the imaging setup, (e) with a 30 µF capacitor bank, and (f) with a 1000 µF capacitor bank. The voltages and currents are displayed for 4 periods of the DF waveform for visualization purposes.

capacitance achieves a current waveform with reduced distortion, shown in Figure 3.8(b). To ensure that the DC current is blocked while keeping distortions at a reasonable level, 1000 µF capacitance is chosen for the capacitor bank.

3.5 Proof-of-Concept Imaging Experiments

Proof-of-concept imaging experiments were performed to demonstrate that imaging at two different frequencies can be performed using the AW drive coils. These imaging experiments were performed on our in-house FFL MPI scanner, shown in Fig. 3.9a. This scanner performed projection format imaging and had selection field gradients of (-4.4,0,4.4) T/m, and a free imaging bore size of 3.6 cm [45]. The implemented AW drive coil is shown in Fig. 3.9b, with the measured specification given in Table 3.1. The receive coil was a tunable gradiometer coil. The imaging procedure is explained in Fig. 3.9c. The DF waveform was sent to a power

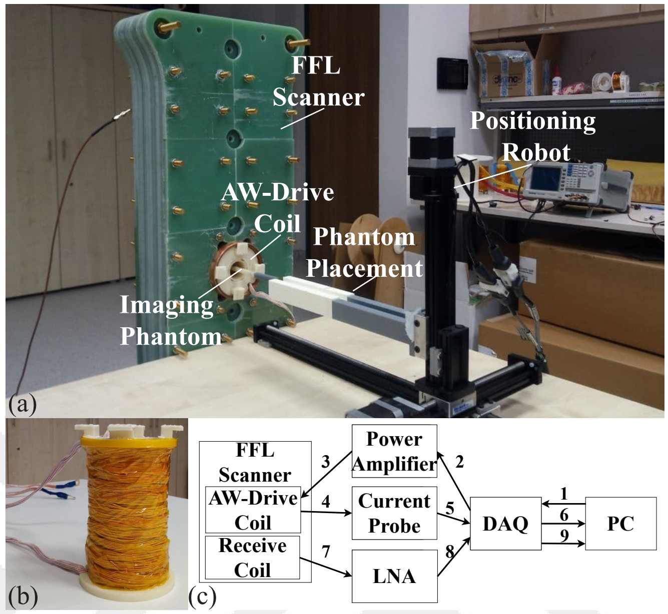

Figure 3.9: (a) In-house FFL MPI scanner and (b) AW drive coil. (c) Imaging procedure. Arrows 1-6: Adjustment of the input voltage according to a baseline acquisition and desired DF amplitude. The PC sends a signal using DAQ to power amplifier, which amplifies the signal and feeds it to AW drive coil. The current through the AW drive coil is measured with a current probe. Arrows 7-9: MPI signal acquisition during imaging.

amplifier (AE Techron 7224) through a data acquisition card (DAQ) (NI USB-6383). The power amplifier was directly connected to the AW drive coil without the need for impedance matching. The current through the AW drive coil was calibrated using a current probe (LFR 06/6/300, PEM) before each experiment. The received signal was amplified with a low-noise voltage pre-amplifier (LNA) (SRS SR560) and sent to a PC via the DAQ. The entire setup was controlled using MATLAB.

The imaging phantom contained two samples: 30 µL 10-fold diluted Perimag MNPs with 1.7 mg Fe/mL concentration and 30 µL undiluted Vivotrax MNPs with 5.5 mg Fe/mL concentration. A 2D line-by-line trajectory was utilized to cover a FOV of size 1.7×5.4 cm^2 in the x-z plane, with a total scan time of 76 s. This FOV was covered in 18 lines along the z-direction, distanced 1 mm apart from each other. Imaging was performed at two different sinusoidal DF waveforms at 2.5 kHz and 5 kHz, with a fixed amplitude of 7 mT. The MPI images were

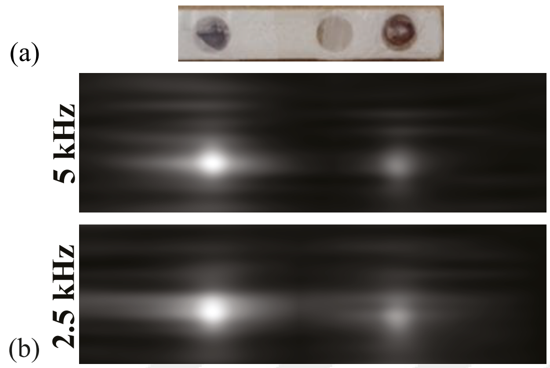

Figure 3.10: Imaging experiment results for AW MPI scanner. (a) The imaging phantom containing two samples placed at 2.3 cm separation. (b) Projection format MPI images at 5 kHz and 2.5 kHz. FOV was $1.7{\times}5.4$ cm^2 in the x-z plane.

reconstructed using Partial FOV Center Imaging (PCI), a robust x-space based reconstruction algorithm [49].

The imaging experiment results are shown in Fig. 3.10, along with the imaging phantom. The signal level at 2.5 kHz was approximately half of that at 5 kHz, which caused slightly increased background artifacts at 2.5 kHz. These results demonstrate that the proposed AW MPI scanner can image successfully at different frequencies without any impedance matching.

Chapter 4

Imaging and Relaxation Mapping at Multiple Frequencies

Parts of this chapter are based on the following publication:

B. Alyuz, M.T. Arslan, M. Utkur and E.U. Saritas, "Single-Pass Relaxation Mapping at Multiple Frequencies using an Arbitrary Waveform MPI Scanner", International Journal on Magnetic Particle Imaging, 9(1 Suppl 1):2303075, 2023.

4.1 Introduction

Magnetic nanoparticles (MNPs) have distinct MPI signals governed by their physical properties in conjunction with the environmental conditions such as temperature and viscosity, enabling identification of MNP type and environmental properties [66, 67]. We have previously proposed a technique called TAURUS (TAU estimation via Recovery of Underlying mirror Symmetry), a relaxation time constant (τ) estimation method that does not require calibration or prior information about MNPs for distinguishing MNP type or environment [63]. Recently, we have developed Rapid TAURUS, a novel extension of TAURUS that enables τ map estimation for rapid and multi-dimensional trajectories [64]. The details of TAURUS and rapid TAURUS were briefly described in Chapter 2.5.

The MNP signal varies depending on different drive field (DF) parameters, causing the optimal DF parameters to vary depending on the quantitative mapping application [43, 33]. In addition, distinguishing different MNP types or their local environments may require measurements at multiple DF settings [33]. Previous studies employed magnetic particle spectrometer (MPS) setups to achieve arbitrary waveform (AW) characteristics that enable operation at any DF frequency [39, 38, 40, 43]. In addition, a small-scale field free line (FFL) MPI scanner was constructed by adding magnets to an AWR to enable pulsed excitation in MPI [41]. In Chapter 4, We presented a low-inductance DF coil design that eliminates conventional methods for reactive power control and capacitates AW characteristics in a typical-size MPI scanner [37].

This chapter proposes a technique for single-pass imaging relaxation mapping at multiple frequencies using an AW MPI scanner. The experimental results are shown through imaging experiments and τ map estimations with Rapid TAURUS on our in-house FFL AW MPI scanner at two different DF frequencies, 5 kHz and 8 kHz, imaged in a single pass by switching the operating DF back and forth.

4.2 Methods

4.2.1 Imaging Setup

The experiments were performed on our in-house AW MPI scanner. This FFL scanner has selection field gradients of (-4.4,0,4.4) T/m and a free bore diameter of 3.6 cm, capable of performing projection format imaging. Our in-house AW MPI scanner, shown in Fig. 4.1, features a low-inductance DF coil, wound using Rutherford cable windings [37]. The AW DF coil parameters were optimized to provide a favorable trade-off between coil sensitivity and coil inductance, enabling operation in a wide band of frequencies within the limits of our power amplifier.

Accordingly, the AW DF coil has 3 layers with 13 Rutherford cable windings per layer, with each cable having a 6×2 wire structure. The AW DF coil has an inner diameter of 4.4 cm and a length of 12 cm. The inductance of the coil was measured to be around 23.8 µH, with a coil sensitivity of 0.27 mT/A. In contrast, a standard DF coil with the same diameter and length but wound using regular Litz wire windings would have 3.56 mH inductance and 3.28 mT/A coil sensitivity. Hence, the AW DF coil provides lower inductance to enable AW characteristics, at the expense of reduced coil sensitivity. Additionally, a capacitor bank was constructed for blocking DC currents on the AW DF coil, as shown in Fig. 3.6(b).

The imaging procedure is explained in Fig. 4.1c. The constructed DF waveform was sent to a power amplifier (AE Techron 7224) through a data acquisition card (DAQ) (NI USB-6383). The power amplifier was directly connected to capacitor bank and the AW DF coil, without any impedance matching circuitry. Before each experiment, the current through the AW DF coil was calibrated using a current probe (LFR 06/6/300, PEM). The received signal was amplified with a low-noise voltage pre-amplifier (LNA) (SRS SR560) and sent to a PC via the DAQ. The entire setup was controlled using MATLAB.

4.2.2 1D Imaging Experiments

First, 1D imaging experiments were performed simultaneously at two different DF settings: (5 kHz,15 mT) and (8 kHz,10 mT). The DF waveform was formed by continuously applying 40 periods of a sinusoidal DF at (5 kHz,15 mT) followed by 40 periods of a sinusoidal DF at (8 kHz,10 mT) repetitively throughout the total scan time.

The imaging phantom contained two samples: 20 µL and 30 µL undiluted Perimag MNPs with 1.7 mgFe/mL concentration, placed at 4.8 cm separation. For 1D imaging experiments, a linear actuator continuously moved the sample in a line, while the multi-frequency DF waveform was applied simultaneously. A 15 cm field-of-view (FOV) was covered in a total scan time of 7.6 s. All measurements were performed at room temperature.

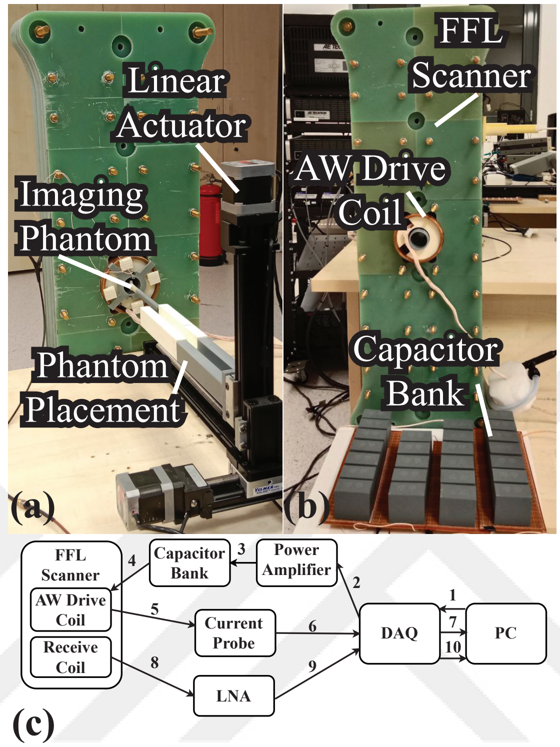

Figure 4.1: Our in-house AW MPI scanner with an FFL topology. (a) Front and (b) back views of the scanner. The AW DF coil features a low inductance of 23.8 µH. The capacitor bank is used for blocking DC currents on the AW DF coil. (c) Signal flowchart showing the imaging procedure. Arrows 1-7: Adjustment of the input voltage according to a baseline acquisition and desired DF amplitude. The PC sends a signal using DAQ to power amplifier, which amplifies the signal and feeds it to AW drive coil. The current through the AW drive coil is measured with a current probe.

4.2.3 2D Imaging Experiments

Next, 2D imaging experiments were performed at the same two DF settingsas in the 1D imaging experiments: (5 kHz,15 mT) and (8 kHz,10 mT). The DF waveform was formed the same way as in 1D experiments by consecutively applying a DF waveform consisting of 40 periods of a sinusoidal DF at (5 kHz,15 mT) and a sinusoidal DF at (8 kHz,10 mT) throughout the total scan time.

The imaging phantom was designed to include samples at varying viscosities. To this end, the phantom contained 3 samples, each having a total volume of

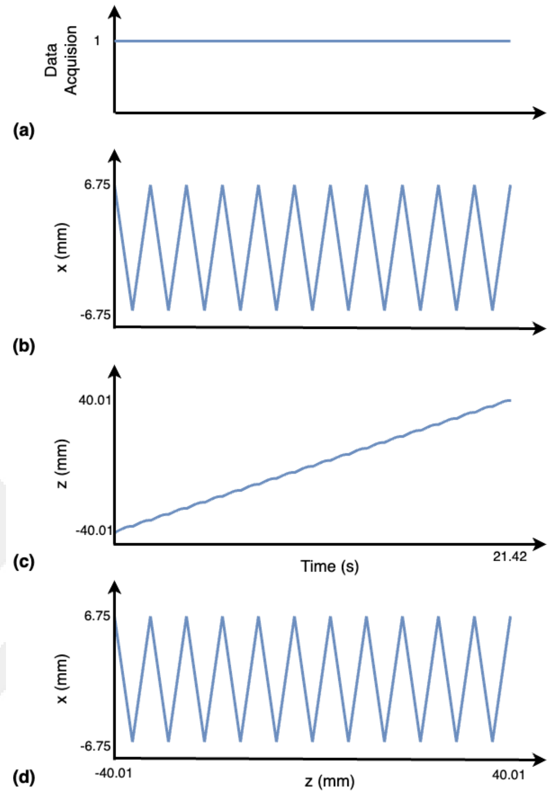

Figure 4.2: The 2D triangle trajectory used in the experiments. (a) The data is acquired continuously throughout the experiment. (b) The movement along the x-axis and (c) the movement along the z-axis with respect to time. (d) The 2D triangle trajectory in z-x plane used in 2D imaging experiments.

60 µL, consisting of 30 µL undiluted Perimag MNPs and varying glycerol and deionized (DI) water volumes. Table 4.1 includes the viscosities and the corresponding glycerol percentages by volume for each sample in the phantom. The prepared samples at different viscosity levels were placed at 2.4 cm separations.

For 2D imaging experiments, an 80.2×13.5 mm^2 FOV in z-x plane was covered in a total scan time of 21.4 s. The imaging sample was moved through the imaging FOV via a linear actuator in a 2D triangle trajectory, shown in Figure 4.2. This trajectory covered the entire FOV in 11 triangles while the multi-frequency DF waveform was applied continuously.

Table 4.1: Samples in the phantom for 2D imaging experiments. Each sample had 60 µL total volume and contained 30 µL of undiluted Perimag MNPs.

	Sample #1	**Sample #2**	**Sample #3**
Viscosity	0.89 mPa·s	2.10 mPa·s	6.89 mPa·s
Glycerol % by Volume	0	25	50

4.2.4 Image and Relaxation Map Reconstruction

For both 1D and 2D imaging experiments, the overall received signal was separated into two parts, extracting the corresponding signal for each DF setting. Next, MPI images were reconstructed separately at each DF setting. For 1D imaging experiments, partial FOV center imaging (PCI), a robust x-space based reconstruction algorithm, was utilized for MPI image reconstruction [49]. The relaxation maps were also reconstructed separately at each DF setting, using Rapid TAURUS [64].

For 2D imaging experiments, the MPI images were reconstructed individually using gridding reconstruction algorithm for non-Cartesian x-space [58]. Additionally, relaxation maps for each DF setting were estimated with Rapid TAURUS algorithm [64]. The estimated τ values were gridded onto a 2D Cartesian grid to obtain the 2D τ maps with the gridding reconstruction algorithm [58].

Relaxation maps were normalized to show percentage τ values with respect to the DF period (i.e., $\hat{\tau} = \tau / T_0 \cdot 100$), to enable comparison of τ from different DF frequencies.

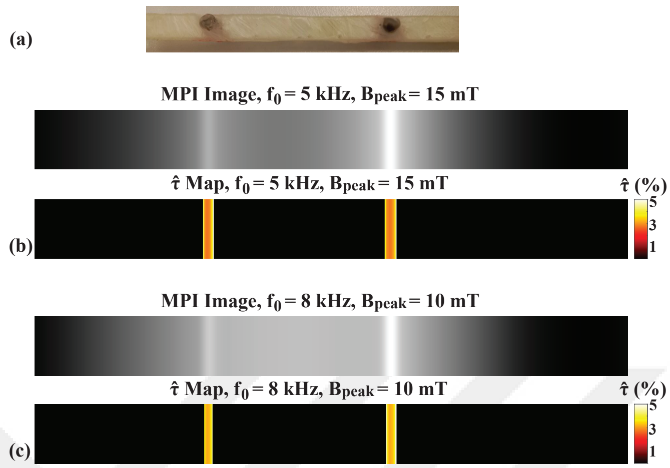

Figure 4.3: Experiment results at (5 kHz,15 mT) and (8 kHz,10 mT), imaged in a single pass using an AW MPI scanner. (a) Imaging phantom containing two Perimag MNP samples. (b) 1D MPI image and 1D $\hat{\tau}$ map at (5 kHz,15 mT). The estimated $\hat{\tau}$ was approximately 2.8%. (c) 1D MPI image and 1D $\hat{\tau}$ map at (8 kHz,10 mT). The estimated $\hat{\tau}$ was approximately 3.2%. Both the MPI images and $\hat{\tau}$ maps were replicated in the vertical direction for display purposes.

4.3 Results

4.3.1 1D Imaging Experiments

The experiment results for the selected DF settings of (5 kHz,15 mT) and (8 kHz,10 mT) are shown in Fig. 4.3. Imaged in a single pass, both DF settings provided successful MPI image reconstruction and relaxation map estimation. These figures show the percentage τ value with respect to the DF period.Accordingly, while the MPI images look almost identical, $\hat{\tau}$ maps can be easily distinguished between the two DF settings: $\hat{\tau}$ was approximately 2.8% at (5 kHz,15 mT) and approximately 3.2% at (8 kHz,10 mT). This relative change in $\hat{\tau}$ between the two DF settings is consistent with the literature, as $\hat{\tau}$ was shown to increase with increasing DF frequency and decreasing DF amplitude [33].

These results demonstrate that the proposed AW MPI scanner can simultaneously image and estimate τ maps at different frequencies in a single imaging pass, thanks to the operating flexibility that it provides. Note that different

Table 4.2: The estimated $\hat{\tau}$ values for each sample in the phantom at each DF setting

	Sample #1	**Sample #2**	**Sample #3**
Viscosity	0.89 mPa·s	2.10 mPa·s	6.89 mPa·s
$\hat{\tau}$ **at (5 kHz,15 mT)**	1.80 %	1.62%	1.41 %
$\hat{\tau}$ **at (8 kHz,10 mT)**	3.45%	3.02 %	2.73 %

MNPs and/or environments may yield identical $\hat{\tau}$ values depending on the DF settings. In addition, environmental factors such as temperature and viscosity may have confounding effects on $\hat{\tau}$ values. Therefore, measurements at two or more DF settings are needed for applications that aim to distinguish different MNP types and their local environments [33]. The proposed approach will be particularly useful for such applications by enabling rapid relaxation mapping at multiple DF settings.

4.3.2 2D Imaging Experiments

The 2D experiment results for the selected DF settings of (5 kHz,15 mT) and (8 kHz,10 mT) are shown in Figure 4.4. The reconstructions and relaxation map estimations were successful for both DF settings. The MPI images look quite similar to one another, however $\hat{\tau}$ maps can be easily distinguished between the two DF settings for three different viscosities.

Table 4.2 shows the estimated $\hat{\tau}$ values at each DF setting. At both DF settings, the $\hat{\tau}$ values decreased with increasing viscosity levels. It was shown in the literature that $\hat{\tau}$ increases with increasing DF frequency and decreasing DF amplitude [33], which also can be observed in the relative change in $\hat{\tau}$ values between the two DF settings in 2D experiments.

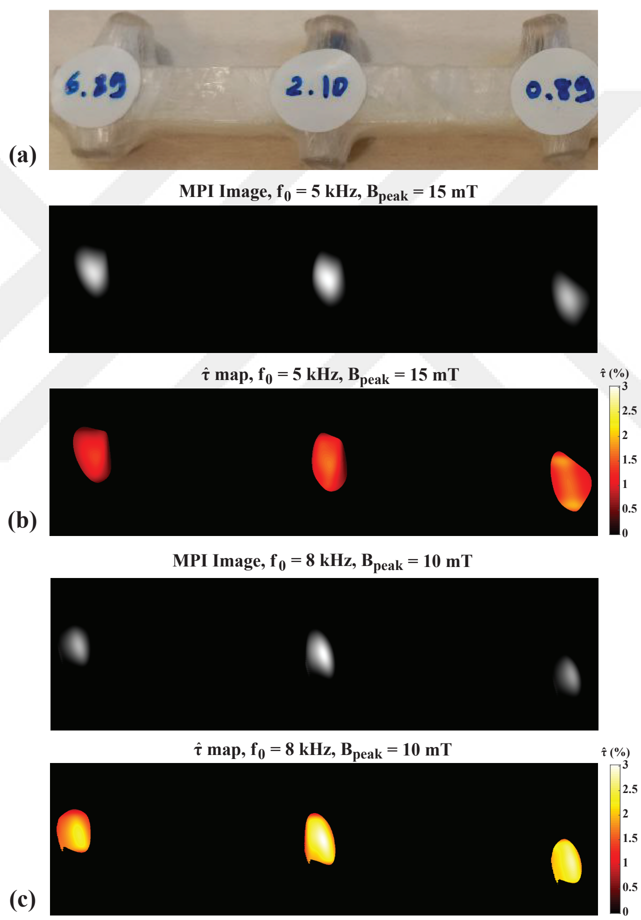

Figure 4.4: 2D Experiment results at (5 kHz,15 mT) and (8 kHz,10 mT), imaged in a single pass using an AW MPI scanner. (a) Imaging phantom containing three Perimag MNP samples at different viscosities. (b) The MPI image and the $\hat{\tau}$ map at (5 kHz,15 mT) (b) MPI image and the $\hat{\tau}$ map at (8 kHz,10 mT).

Chapter 5

Conclusion and Future Work

In this thesis, a novel design for a preclinical MPI scanner that can operate in a wide bandwidth without the need of impedance matching or tuning circuitry was presented. The design achieves the AW characteristics in an MPI scanner of preclinical size by reducing the inductance of the drive coil using Rutherford cable windings. With this cable winding, the inductance of the AW drive coil was reduced approximately 144-fold and the voltage required to generate a DF was reduced 12-fold. The results show that the preclinical AW MPI scanner is able to perform imaging at various frequencies without any alterations in the imaging setup. The ability to operate in a range of frequencies provides a beneficial practicality and adaptability for functional imaging applications in MPI.

In addition, in this thesis, a multi-frequency imaging technique for obtaining MPI images and relaxation maps at multiple DF settings in a single scan was proposed. The results for 1D and 2D imaging experiments show that the proposed imaging procedure can obtain the MPI image and estimate the relaxation maps successfully at multiple DF settings in a single experiment using the AW MPI scanner. Measurements at two or more DF settings are needed for applications that aim to distinguish different MNP types and their local environments since different MNPs and/or environments may produce identical τ estimations if tested at a single DF setting. The proposed imaging procedure can enable rapid relaxation mapping at multiple DF settings, which can facilitate the characterization of MNP type and environment.

As a future work, the number of DF settings obtained in a single experiment can be increased by employing denser and/or more complex scanning trajectories. The heating of the components of the AW MPI scanner and the MNP heating due to increased scan time along with the sampling rate for each DF setting must be considered when designing an experiment to incorporate more DF settings in a single-pass for imaging and relaxation mapping.

As an extension of this approach, magnetic particle fingerprinting (MPF) experiments can be performed for MPI in a single experiment using AW MPI scanner. The MPF teachnique swiftly covers a wide range of DF parameters while mapping the unique τ-fingerprint of the sample, and allows for rapid relaxation mapping of the MNPs [43]. The relaxation behavior of the MNPs can be observed for a wider range of DF parameters with the AW MPI scannner with less modifications to the imaging setup.

Bibliography

[1] T. Knopp and T. M. Buzug, *Magnetic particle imaging: an introduction to imaging principles and scanner instrumentation*. Springer Science & Business Media, 2012.

[2] B. Gleich and J. Weizenecker, "Tomographic imaging using the nonlinear response of magnetic particles," *Nature*, vol. 435, no. 7046, pp. 1214–1217, 2005.

[3] E. U. Saritas, P. W. Goodwill, L. R. Croft, J. J. Konkle, K. Lu, B. Zheng, and S. M. Conolly, "Magnetic particle imaging (mpi) for nmr and mri researchers," *Journal of Magnetic Resonance*, vol. 229, pp. 116–126, 2013.

[4] J. Weizenecker, J. Borgert, and B. Gleich, "A simulation study on the resolution and sensitivity of magnetic particle imaging," *Physics in Medicine & Biology*, vol. 52, no. 21, p. 6363, 2007.

[5] J. Weizenecker, B. Gleich, J. Rahmer, H. Dahnke, and J. Borgert, "Three-dimensional real-time in vivo magnetic particle imaging," *Physics in Medicine & Biology*, vol. 54, no. 5, p. L1, 2009.

[6] K. Lu, P. W. Goodwill, E. U. Saritas, B. Zheng, and S. M. Conolly, "Linearity and shift invariance for quantitative magnetic particle imaging," *IEEE transactions on medical imaging*, vol. 32, no. 9, pp. 1565–1575, 2013.

[7] B. Zheng, T. Vazin, P. W. Goodwill, A. Conway, A. Verma, E. Ulku Saritas, D. Schaffer, and S. M. Conolly, "Magnetic particle imaging tracks the long-term fate of in vivo neural cell implants with high image contrast," *Scientific reports*, vol. 5, no. 1, p. 14055, 2015.

[8] B. Zheng, M. P. von See, E. Yu, B. Gunel, K. Lu, T. Vazin, D. V. Schaffer, P. W. Goodwill, and S. M. Conolly, "Quantitative magnetic particle imaging monitors the transplantation, biodistribution, and clearance of stem cells in vivo," *Theranostics*, vol. 6, no. 3, p. 291, 2016.

[9] K. Them, J. Salamon, P. Szwargulski, S. Sequeira, M. Kaul, C. Lange, H. Ittrich, and T. Knopp, "Increasing the sensitivity for stem cell monitoring in system-function based magnetic particle imaging," *Physics in Medicine & Biology*, vol. 61, no. 9, p. 3279, 2016.

[10] J. Haegele, J. Rahmer, B. Gleich, J. Borgert, H. Wojtczyk, N. Panagiotopoulos, T. M. Buzug, J. Barkhausen, and F. M. Vogt, "Magnetic particle imaging: visualization of instruments for cardiovascular intervention," *Radiology*, vol. 265, no. 3, pp. 933–938, 2012.

[11] E. Y. Yu, M. Bishop, B. Zheng, R. M. Ferguson, A. P. Khandhar, S. J. Kemp, K. M. Krishnan, P. W. Goodwill, and S. M. Conolly, "Magnetic particle imaging: a novel in vivo imaging platform for cancer detection," *Nano letters*, vol. 17, no. 3, pp. 1648–1654, 2017.

[12] Z. W. Tay, P. Chandrasekharan, X. Y. Zhou, E. Yu, B. Zheng, and S. Conolly, "In vivo tracking and quantification of inhaled aerosol using magnetic particle imaging towards inhaled therapeutic monitoring," *Theranostics*, vol. 8, no. 13, p. 3676, 2018.

[13] X. Zhu, J. Li, P. Peng, N. Hosseini Nassab, and B. R. Smith, "Quantitative drug release monitoring in tumors of living subjects by magnetic particle imaging nanocomposite," *Nano letters*, vol. 19, no. 10, pp. 6725–6733, 2019.

[14] Z. W. Tay, P. Chandrasekharan, A. Chiu-Lam, D. W. Hensley, R. Dhavalikar, X. Y. Zhou, E. Y. Yu, P. W. Goodwill, B. Zheng, C. Rinaldi, *et al.*, "Magnetic particle imaging-guided heating in vivo using gradient fields for arbitrary localization of magnetic hyperthermia therapy," *ACS nano*, vol. 12, no. 4, pp. 3699–3713, 2018.

[15] E. U. Saritas, P. W. Goodwill, G. Z. Zhang, and S. M. Conolly, "Magnetostimulation limits in magnetic particle imaging," *IEEE transactions on medical imaging*, vol. 32, no. 9, pp. 1600–1610, 2013.

[16] I. Schmale, B. Gleich, J. Rahmer, C. Bontus, J. Schmidt, and J. Borgert, "Mpi safety in the view of mri safety standards," *IEEE Transactions on Magnetics*, vol. 51, no. 2, pp. 1–4, 2015.

[17] P. W. Goodwill, J. J. Konkle, B. Zheng, E. U. Saritas, and S. M. Conolly, "Projection x-space magnetic particle imaging," *IEEE transactions on medical imaging*, vol. 31, no. 5, pp. 1076–1085, 2012.

[18] P. Goodwill, L. Croft, J. Konkle, K. Lu, E. Saritas, B. Zheng, and S. Conolly, "Third generation x-space mpi mouse and rat scanner," in *Magnetic Particle Imaging: A Novel SPIO Nanoparticle Imaging Technique*, pp. 261–265, Springer, 2012.

[19] P. W. Goodwill, L. R. Croft, J. J. Konkle, K. Lu, E. U. Saritas, B. Zheng, and S. M. Conolly, "A 7 t/m 3d x-space mpi mouse and rat scanner," in *2013 International Workshop on Magnetic Particle Imaging (IWMPI)*, pp. 1–1, IEEE, 2013.

[20] J. Rahmer, J. Weizenecker, B. Gleich, and J. Borgert, "Signal encoding in magnetic particle imaging: properties of the system function," *BMC medical imaging*, vol. 9, pp. 1–21, 2009.

[21] T. Knopp, J. Rahmer, T. F. Sattel, S. Biederer, J. Weizenecker, B. Gleich, J. Borgert, and T. M. Buzug, "Weighted iterative reconstruction for magnetic particle imaging," *Physics in medicine & biology*, vol. 55, no. 6, p. 1577, 2010.

[22] P. W. Goodwill and S. M. Conolly, "The x-space formulation of the magnetic particle imaging process: 1-d signal, resolution, bandwidth, snr, sar, and magnetostimulation," *IEEE transactions on medical imaging*, vol. 29, no. 11, pp. 1851–1859, 2010.

[23] P. W. Goodwill and S. M. Conolly, “Multidimensional x-space magnetic particle imaging,” *IEEE transactions on medical imaging*, vol. 30, no. 9, pp. 1581–1590, 2011.

[24] L. R. Croft, P. W. Goodwill, and S. M. Conolly, “Relaxation in x-space magnetic particle imaging,” *IEEE transactions on medical imaging*, vol. 31, no. 12, pp. 2335–2342, 2012.

[25] J. Haegele, S. Vaalma, N. Panagiotopoulos, J. Barkhausen, F. M. Vogt, J. Borgert, and J. Rahmer, “Multi-color magnetic particle imaging for cardiovascular interventions,” *Physics in Medicine & Biology*, vol. 61, no. 16, p. N415, 2016.

[26] J. Rahmer, D. Wirtz, C. Bontus, J. Borgert, and B. Gleich, “Interactive magnetic catheter steering with 3-d real-time feedback using multi-color magnetic particle imaging,” *IEEE transactions on medical imaging*, vol. 36, no. 7, pp. 1449–1456, 2017.

[27] N. Nothnagel, J. Rahmer, B. Gleich, A. Halkola, T. M. Buzug, and J. Borgert, “Steering of magnetic devices with a magnetic particle imaging system,” *IEEE Transactions on Biomedical Engineering*, vol. 63, no. 11, pp. 2286–2293, 2016.

[28] M. Utkur, Y. Muslu, and E. U. Saritas, “Relaxation-based viscosity mapping for magnetic particle imaging,” *Physics in Medicine & Biology*, vol. 62, no. 9, p. 3422, 2017.

[29] C. Shasha, E. Teeman, and K. M. Krishnan, “Harmonic simulation study of simultaneous nanoparticle size and viscosity differentiation,” *IEEE Magnetics Letters*, vol. 8, pp. 1–5, 2017.

[30] M. Möddel, C. Meins, J. Dieckhoff, and T. Knopp, “Viscosity quantification using multi-contrast magnetic particle imaging,” *New journal of physics*, vol. 20, no. 8, p. 083001, 2018.

[31] M. Utkur, Y. Muslu, and E. U. Saritas, “Relaxation-based color magnetic particle imaging for viscosity mapping,” *Applied Physics Letters*, vol. 115, no. 15, 2019.

[32] S. Draack, M. Schilling, and T. Viereck, “Magnetic particle imaging of particle dynamics in complex matrix systems,” *Physical Sciences Reviews*, vol. 8, no. 2, pp. 213–237, 2021.

[33] M. Utkur and E. U. Saritas, “Simultaneous temperature and viscosity estimation capability via magnetic nanoparticle relaxation,” *Medical Physics*, vol. 49, no. 4, pp. 2590–2601, 2022.

[34] C. Stehning, B. Gleich, and J. Rahmer, “Simultaneous magnetic particle imaging (mpi) and temperature mapping using multi-color mpi,” *International Journal on Magnetic Particle Imaging IJMPI*, vol. 2, no. 2, 2016.

[35] J. Zhong, M. Schilling, and F. Ludwig, “Magnetic nanoparticle temperature imaging with a scanning magnetic particle spectrometer,” *Measurement Science and Technology*, vol. 29, no. 11, p. 115903, 2018.

[36] Y. Shi and J. B. Weaver, “Concurrent quantification of magnetic nanoparticles temperature and relaxation time,” *Medical physics*, vol. 46, no. 9, pp. 4070–4076, 2019.

[37] B. Alyüz, M. T. Arslan, M. Utkur, and E. U. Saritas, “An arbitrary waveform mpi scanner,” *International Journal on Magnetic Particle Imaging IJMPI*, vol. 8, no. 1 Suppl 1, 2022.

[38] Z. W. Tay, P. W. Goodwill, D. W. Hensley, L. A. Taylor, B. Zheng, and S. M. Conolly, “A high-throughput, arbitrary-waveform, mpi spectrometer and relaxometer for comprehensive magnetic particle optimization and characterization,” *Scientific reports*, vol. 6, no. 1, p. 34180, 2016.

[39] C. B. TOP, “An arbitrary waveform magnetic nanoparticle relaxometer with an asymmetrical three-section gradiometric receive coil,” *Turkish journal of electrical engineering and computer sciences*, vol. 28, no. 3, pp. 1344–1354, 2020.

[40] D. Pantke, N. Holle, A. Mogarkar, M. Straub, and V. Schulz, “Multifrequency magnetic particle imaging enabled by a combined passive and active drive field feed-through compensation approach,” *Medical physics*, vol. 46, no. 9, pp. 4077–4086, 2019.

[41] Z. W. Tay, D. Hensley, J. Ma, P. Chandrasekharan, B. Zheng, P. Goodwill, and S. Conolly, "Pulsed excitation in magnetic particle imaging," *IEEE transactions on medical imaging*, vol. 38, no. 10, pp. 2389–2399, 2019.

[42] B. Alyuz, M. T. Arslan, M. Utkur, and E. U. Saritas, "Single-pass relaxation mapping at multiple frequencies using an arbitrary waveform mpi scanner," *International Journal on Magnetic Particle Imaging IJMPI*, vol. 9, no. 1 Suppl 1, 2023.

[43] E. Yagiz, M. Utkur, C. B. Top, and E. U. Saritas, "Magnetic particle fingerprinting using arbitrary waveform relaxometer," *International Journal on Magnetic Particle Imaging IJMPI*, vol. 6, no. 2 Suppl 1, 2020.

[44] T. M. Buzug, G. Bringout, M. Erbe, K. Gräfe, M. Graeser, M. Grüttner, A. Halkola, T. F. Sattel, W. Tenner, H. Wojtczyk, *et al.*, "Magnetic particle imaging: Introduction to imaging and hardware realization," *Zeitschrift für Medizinische Physik*, vol. 22, no. 4, pp. 323–334, 2012.

[45] A. R. Çağıl and E. U. Saritas, "Design of a preclinical field free point/field free line hybrid mpi scanner," *IWMPI*, 2019.

[46] C. B. Top, S. Ilbey, and H. E. Güven, "Electronically rotated and translated field-free line generation for open bore magnetic particle imaging," *Medical Physics*, vol. 44, no. 12, pp. 6225–6238, 2017.

[47] N. Panagiotopoulos, R. L. Duschka, M. Ahlborg, G. Bringout, C. Debbeler, M. Graeser, C. Kaethner, K. Lüdtke-Buzug, H. Medimagh, J. Stelzner, *et al.*, "Magnetic particle imaging: current developments and future directions," *International journal of nanomedicine*, pp. 3097–3114, 2015.

[48] M. Graeser, T. Knopp, P. Szwargulski, T. Friedrich, A. Von Gladiß, M. Kaul, K. M. Krishnan, H. Ittrich, G. Adam, and T. M. Buzug, "Towards picogram detection of superparamagnetic iron-oxide particles using a gradiometric receive coil," *Scientific reports*, vol. 7, no. 1, p. 6872, 2017.

[49] S. Kurt, Y. Muslu, and E. U. Saritas, "Partial fov center imaging (pci): a robust x-space image reconstruction for magnetic particle imaging," *IEEE transactions on medical imaging*, vol. 39, no. 11, pp. 3441–3450, 2020.

[50] L. Yin, W. Li, Y. Du, K. Wang, Z. Liu, H. Hui, and J. Tian, "Recent developments of the reconstruction in magnetic particle imaging," *Visual computing for industry, biomedicine, and art*, vol. 5, no. 1, p. 24, 2022.

[51] T. Knopp, T. F. Sattel, S. Biederer, J. Rahmer, J. Weizenecker, B. Gleich, J. Borgert, and T. M. Buzug, "Model-based reconstruction for magnetic particle imaging," *IEEE Transactions on Medical Imaging*, vol. 29, no. 1, pp. 12–18, 2009.

[52] T. Knopp, S. Biederer, T. F. Sattel, J. Rahmer, J. Weizenecker, B. Gleich, J. Borgert, and T. M. Buzug, "2d model-based reconstruction for magnetic particle imaging," *Medical physics*, vol. 37, no. 2, pp. 485–491, 2010.

[53] T. Knopp and A. Weber, "Sparse reconstruction of the magnetic particle imaging system matrix," *IEEE transactions on medical imaging*, vol. 32, no. 8, pp. 1473–1480, 2013.

[54] A. Weber, T. Knopp, *et al.*, "Reconstruction of the magnetic particle imaging system matrix using symmetries and compressed sensing," *Advances in Mathematical Physics*, vol. 2015, 2015.

[55] S. Ilbey, C. B. Top, A. Güngör, T. Çukur, E. U. Saritas, and H. E. Güven, "Fast system calibration with coded calibration scenes for magnetic particle imaging," *IEEE Transactions on Medical Imaging*, vol. 38, no. 9, pp. 2070–2080, 2019.

[56] S. Ilbey, C. B. Top, A. Güngör, T. Çukur, E. U. Saritas, and H. E. Güven, "Comparison of system-matrix-based and projection-based reconstructions for field free line magnetic particle imaging," *International Journal on Magnetic Particle Imaging IJMPI*, vol. 3, no. 1, 2017.

[57] D. Sarica, Ö. B. Demirel, and E. Ü. Saritaş, "Dc shift based image reconstruction for magnetic particle imaging," in *2017 25th Signal Processing and Communications Applications Conference (SIU)*, pp. 1–4, IEEE, 2017.

[58] A. Ozaslan, A. Alacaoglu, O. Demirel, T. Çukur, and E. Saritas, "Fully automated gridding reconstruction for non-cartesian x-space magnetic particle imaging," *Physics in Medicine & Biology*, vol. 64, no. 16, p. 165018, 2019.

[59] K. Bente, M. Weber, M. Graeser, T. F. Sattel, M. Erbe, and T. M. Buzug, “Electronic field free line rotation and relaxation deconvolution in magnetic particle imaging,” *IEEE transactions on medical imaging*, vol. 34, no. 2, pp. 644–651, 2014.

[60] S. A. Shah, D. B. Reeves, R. M. Ferguson, J. B. Weaver, and K. M. Krishnan, “Mixed brownian alignment and néel rotations in superparamagnetic iron oxide nanoparticle suspensions driven by an ac field,” *Physical Review B*, vol. 92, no. 9, p. 094438, 2015.

[61] R. E. Rosensweig, “Heating magnetic fluid with alternating magnetic field,” *Journal of magnetism and magnetic materials*, vol. 252, pp. 370–374, 2002.

[62] S. Ota and Y. Takemura, “Characterization of néel and brownian relaxations isolated from complex dynamics influenced by dipole interactions in magnetic nanoparticles,” *The Journal of Physical Chemistry C*, vol. 123, no. 47, pp. 28859–28866, 2019.

[63] Y. Muslu, M. Utkur, O. B. Demirel, and E. U. Saritas, “Calibration-free relaxation-based multi-color magnetic particle imaging,” *IEEE transactions on medical imaging*, vol. 37, no. 8, pp. 1920–1931, 2018.

[64] M. T. Arslan, A. A. Özaslan, S. Kurt, Y. Muslu, and E. U. Saritas, “Rapid taurus for relaxation-based color magnetic particle imaging,” *IEEE Transactions on Medical Imaging*, vol. 41, no. 12, pp. 3774–3786, 2022.

[65] A. A. Ozaslan, A. R. Cagil, M. Graeser, T. Knopp, and E. U. Saritas, “Design of a magnetostimulation head coil with rutherford cable winding,” *International Journal on Magnetic Particle Imaging*, vol. 6, no. 2 Suppl 1, 2020.

[66] A. M. Rauwerdink and J. B. Weaver, “Viscous effects on nanoparticle magnetization harmonics,” *Journal of Magnetism and Magnetic Materials*, vol. 322, no. 6, pp. 609–613, 2010.

[67] M. Möddel, C. Meins, J. Dieckhoff, and T. Knopp, “Viscosity quantification using multi-contrast magnetic particle imaging,” *New Journal of Physics*, vol. 20, p. 083001, aug 2018.